Monthly Notices
of the
ROYAL ASTRONOMICAL SOCIETY

MNRAS **458,** 2745–2761 (2016)
Advance Access publication 2016 March 3

doi:10.1093/mnras/stw470

Evidence for an evolving cyclotron line energy in 4U 1538−522

Paul B. Hemphill,[1⋆] Richard E. Rothschild,[1] Felix Fürst,[2] Victoria Grinberg,[3] Dmitry Klochkov,[4] Peter Kretschmar,[5] Katja Pottschmidt,[6,7] Rüdiger Staubert[4] and Jörn Wilms[8]

[1]*Center for Astrophysics and Space Sciences, University of California, San Diego, 9500 Gilman Dr, La Jolla, CA 92093-0424, USA*
[2]*Cahill Center for Astronomy and Astrophysics, California Institute of Technology, MC 290-17, 1200 E. California Blvd, Pasadena, CA 91125, USA*
[3]*Massachusetts Institute of Technology, Kavli Institute for Astrophysics, Cambridge, MA 02139, USA*
[4]*Institut für Astronomie und Astrophysik, Universität Tübingen (IAAT), Sand 1, D-72076 Tübingen, Germany*
[5]*European Space Astronomy Center (ESA/ESAC), Science Operations Deparment, Villanueva de la Cañada, E-28691 Madrid, Spain*
[6]*Center for Space Science and Technology, University of Maryland Baltimore County, 1000 Hilltop Circle, Baltimore, MD 21250, USA*
[7]*CRESST and NASA Goddard Space Flight Center, Astrophysics Science Division, Code 661, Greenbelt, MD 20771, USA*
[8]*Dr Karl Remeis-Sternwarte and Erlangen Center for Astroparticle Physics, Sternwartstr. 7, D-96049 Bamberg, Germany*

Accepted 2016 February 25. Received 2016 February 4; in original form 2015 December 3

ABSTRACT

We have performed a full time and luminosity-resolved spectral analysis of the high-mass X-ray binary 4U 1538−522 using the available *RXTE*, *INTEGRAL*, and *Suzaku* data, examining both phase-averaged and pulse-phase-constrained data sets and focusing on the behaviour of the cyclotron resonance scattering feature (CRSF). No statistically significant trend between the energy of the CRSF and luminosity is observed in the combined data set. However, the CRSF energy appears to have increased by ∼1.5 keV in the ∼8.5 yr between the *RXTE* and *Suzaku* measurements, with Monte Carlo simulations finding the *Suzaku* measurement 4.6σ above the *RXTE* points. Interestingly, the increased *Suzaku* CRSF energy is much more significant and robust in the pulse-phase-constrained spectra from the peak of the main pulse, suggesting a change that is limited to a single magnetic pole. The seven years of *RXTE* measurements do not show any strongly significant evolution with time on their own. We discuss the significance of the CRSF's behaviour with respect to luminosity and time in the context of historical observations of this source as well as recent observational and theoretical work concerning the neutron star accretion column, and suggest some mechanisms by which the observed change over time could occur.

Key words: accretion, accretion discs – stars: magnetic field – pulsars: individual: 4U 1538−522 – X-rays: binaries – X-rays: stars.

1 INTRODUCTION

Many neutron stars (NS) possess magnetic fields with dipole strengths in excess of 10^{12} G, making them some of the strongest magnets in the Universe. Material that falls on to the NS is channelled along the field lines and is concentrated on to the magnetic poles, forming a hot, dense column of accreted plasma. The conditions within this accretion column are extreme: the infalling material comes in at relativistic ($v \sim 0.5c$) velocities and must come to a halt by the time it reaches the NS surface. Radiation pressure in the column can play a significant role here, shaping the dynamics of the column, which in turn influences the observed radiation spectrum (see e.g. Becker et al. 2012).

Cyclotron resonance scattering features (CRSFs, also referred to as 'cyclotron lines') are pseudo-absorption features found in the hard X-ray spectra of approximately two dozen accreting X-ray pulsars. The first CRSF was discovered in Hercules X-1 by Trümper et al. (1978). CRSFs appear as a result of the quantized nature of electron cyclotron motion in the characteristically strong magnetic field of young pulsars, which creates resonances in the electron–photon scattering cross-section at the cyclotron line energies and scatters photons out of the line of sight. These features are notable for being the only direct means of measuring the field strength of the NS, as their centroid energy is directly proportional to the field strength in the scattering region.

The last several years have seen a great deal of activity around cyclotron lines, mainly focused on the variation of the CRSF energy with luminosity. The Be/X-ray binary V 0332+53 displays a significant negative correlation between CRSF energy and luminosity (Mowlavi et al. 2006; Tsygankov, Lutovinov & Serber 2010), while

⋆ E-mail: pbhemphill@physics.ucsd.edu

Her X-1 (Staubert et al. 2007) and GX 304-1 (Yamamoto et al. 2011; Klochkov et al. 2012) show positive correlations. This relationship can be complex: *NuSTAR* observations of Vela X-1 (Fürst et al. 2014) found that the energy of the first harmonic of the CRSF was positively correlated with luminosity, while the behaviour of the fundamental was more difficult to discern, while A 0535+26's CRSF is fairly constant at most luminosities (Caballero et al. 2007) but does display a positive correlation between the CRSF energy and flux in certain pulse phase bins (Klochkov et al. 2011; Müller et al. 2013b). A 0535+26 may also have a positive correlation in phase-averaged spectra at its highest luminosities (Sartore, Jourdain & Roques 2015).

A superb, well-studied example of complicated CRSF behaviour can be found in Her X-1, whose CRSF shows a positive $E_{\rm cyc}$–luminosity correlation (Staubert et al. 2007; Vasco, Klochkov & Staubert 2011), variability with pulse phase (Vasco et al. 2013), and variation with the phase of Her X-1's 35 d superorbital period. Most recently, Staubert et al. (2014) showed that for Her X-1, on top of all these observed trends, there is additional variability in the CRSF energy that can only be explained by a long-term decrease in the CRSF energy. Recent *NuSTAR* observations of Her X-1 have confirmed this trend (Fürst et al. 2013). This result suggests that there is the possibility for some long-term evolution within the accretion column that is not observable either in the overall spectral shape or the luminosity of the source.

The accreting X-ray pulsar 4U 1538−522 was discovered by the *Uhuru* satellite (Giacconi et al. 1974), and the system was identified as an X-ray pulsar by Becker et al. (1977), Davison (1977), and Davison, Watson & Pye (1977). The system consists of an $\sim$1 $M_\odot$ NS accreting from the stellar wind of QV Nor, an $\sim$16 $M_\odot$ B0Iab star (Reynolds, Bell & Hilditch 1992; Rawls et al. 2011; Falanga et al. 2015). Estimates of 4U 1538−522's distance have ranged from 4.5 kpc (Clark 2004) to 6.4 $\pm$ 1.0 kpc (Reynolds et al. 1992), with older measurements by Crampton, Hutchings & Cowley (1978) and Ilovaisky, Chevalier & Motch (1979) finding 6.0 $\pm$ 0.5 and 5.5 $\pm$ 1.5 kpc, respectively. The system's binary parameters have similarly been difficult to constrain: while the 3.7 d orbital period was established by some of the earliest observations (Becker et al. 1977; Davison et al. 1977), the orbital parameters found by Makishima et al. (1987), Clark (2000), and Mukherjee et al. (2006) disagree on whether this orbit is circular or elliptical. While we adopt an eccentricity of 0.174 $\pm$ 0.015 from Clark (2000) and Mukherjee et al. (2006), we note that this choice has only minimal effects on this analysis. Interestingly, Rawls et al. (2011) estimated the NS mass to be 0.874 $\pm$ 0.073 $M_\odot$ when using the elliptical orbital solution and 1.104 $\pm$ 0.177 $M_\odot$ for a circular orbit – using either orbital solution, their results clearly suggest that 4U 1538−522 contains a surprisingly low-mass NS.

The pulse period of 4U 1538−522 has an interesting history. Around the time of its discovery, its pulse period was 528.93 $\pm$ 0.10 s (Becker et al. 1977); over the next decade this increased to at least 530.43 $\pm$ 0.014 s (Makishima et al. 1987; Corbet, Woo & Nagase 1993), but observations by the Compton Gamma-Ray Observatory revealed that the source underwent a torque reversal sometime in 1989 or 1990 (Rubin et al. 1997). The spin-up trend continued (Clark 2000; Coburn 2001; Baykal, İnam & Beklen 2006; Mukherjee et al. 2006) for approximately 20 yr, until another torque reversal in $\sim$2008 put the source on its current spin-down trend, as revealed by *Fermi*-GBM[1] (Finger et al. 2009), *INTEGRAL* (Hemphill et al. 2013), and *Suzaku* (Hemphill et al. 2014). The pulse period is currently $\sim$526 s.

4U 1538−522's $\sim$20 keV CRSF was discovered by Clark et al. (1990) in *Ginga* observations. The *Ginga* spectra were further analysed by Makishima et al. (1987). The feature has since been observed in data from the *Rossi X-ray Timing Explorer* (*RXTE*; Coburn 2001; Rodes-Roca et al. 2009), *BeppoSAX* (Robba et al. 2001), *INTEGRAL* (Rodes-Roca et al. 2009; Hemphill et al. 2013), and *Suzaku* (Hemphill et al. 2014). A direct comparison of these results is somewhat difficult, as the various authors used different models for the spectral continuum and the CRSF, as well as different energy bands when calculating fluxes. Discussions of the effects of model choice on the measured CRSF energy can be found in Müller et al. (2013a) and Hemphill et al. (2013). However, limiting ourselves to results using the same models, there is a noticeable change between the early *RXTE* observations in 1996–1997, which found the CRSF at $20.66^{+0.05}_{-0.06}$ keV (Coburn 2001), and the 2012 observation by *Suzaku*, where Hemphill et al. (2014) found the feature at $22.2^{+0.8}_{-0.7}$ keV. It should be noted, however, that the early *RXTE* spectral fit of Coburn (2001) had a very poor reduced χ^2 of $\sim$2.2, so its small error bars should not be viewed as authoritative.

In this paper, we re-analyse the archival *RXTE*, *INTEGRAL*, and *Suzaku* observations of 4U 1538−522 using consistent spectral models to better understand and quantify this apparent trend. We also produce the best-yet characterization of the CRSF's variability with luminosity. After a summary of the data used and the data reduction procedure in Section 2 and a brief timing analysis of the source in Section 3, we present our spectral analysis and results in Sections 4 and 5. A discussion of these results in the context of recent theoretical work can be found in Section 6. All plots display 90 per cent error bars, and we generally present 1σ (68 per cent) confidence intervals on linear fits to our results, unless otherwise indicated.

2 OBSERVATIONS AND DATA ANALYSIS

A search of the NASA High Energy Astrophysics Science Archive finds 70 *RXTE* observation IDs (obsids) containing 4U 1538−522 between the years 1996 and 2004. There is additionally a single *Suzaku* observation from 2012. We supplement our results with $\sim$700 ks of *INTEGRAL* data lying mostly between the *RXTE* and *Suzaku* observations; more in-depth analyses of the available *INTEGRAL* data can be found in Rodes-Roca et al. (2009) and Hemphill et al. (2013). Overall, our data set for 4U 1538−522 spans 16 yr, from the earliest *RXTE* observations in 1996 to the 2012 *Suzaku* observation. We summarize the analysed observations of 4U 1538−522 in Table 1. The *RXTE*, *INTEGRAL*, and *Suzaku* light curves are plotted in Fig. 1.

Unless otherwise stated, all spectral and light curve analysis was performed using version 1.6.2-30 of the Interactive Spectral Interpretation System (ISIS; Houck & Denicola 2000).

2.1 *RXTE* data

RXTE (Bradt, Rothschild & Swank 1993) carried two instruments relevant to this study: the Proportional Counter Array (PCA; Jahoda et al. 1996, 2006), a set of five proportional counter units (PCU 0–4) with a nominal energy range of 2–60 keV, and the High Energy X-ray Timing Experiment (HEXTE; Rothschild et al. 1998), which consists of two independent clusters of phoswich scintillation detectors (HEXTE-A and HEXTE-B), each with an energy range of 15–250 keV. The HEXTE detectors rocked between on-source and

[1] See http://gammaray.nsstc.nasa.gov/gbm/science/pulsars

Table 1. *RXTE*, *Suzaku*, and *INTEGRAL* observations of 4U 1538−522.

Observation	Start (MJD)	End (MJD)	Exposure (ks)	
RXTE proposal			PCA	HEXTE
10145	50450.62	50453.63	114.1	72.9
20146	50411.96	50795.15	56.4	36.8
50067	51924.88	51928.39	99.1	65.0
80016	52851.95	52858.35	53.4	36.3
INTEGRAL revolutions			JEM-X 1	ISGRI
0200–0299	53198.10	53439.40	84.6	234.0
0300–0399	53465.10	53620.90	39.6	107.1
0700–0799	54747.90	54928.60	77.2	240.2
0900–0999	55252.70	55288.90	20.5	127.3
Suzaku obsID			XIS 0	HXD/PIN
407068010	56149.02	56149.73	46.0	36.3

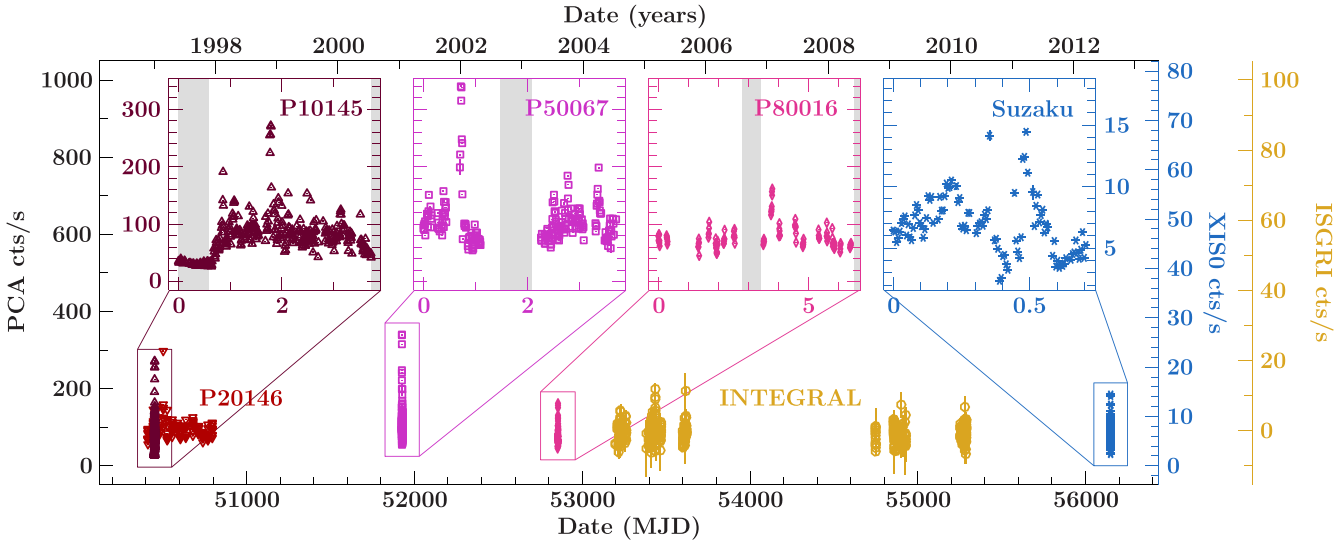

Figure 1. The 3–60 keV *RXTE*-PCA (PCU2), 20–40 keV *INTEGRAL*-ISGRI, and 1–10 keV *Suzaku*-XIS0 light curves. The *RXTE* and *Suzaku* light curves are binned at the pulse period (see Table 3), while the *INTEGRAL* data are binned at 10 times the pulse period. *RXTE* proposals P10145, P20146, P50067, and P80016 are plotted in dark red triangles, red inverted triangles, violet squares, and pink diamonds, respectively, while *INTEGRAL* is plotted in gold circles and *Suzaku* is plotted using blue stars. The inset plots zoom in on the three focused *RXTE* proposals and the *Suzaku* observation, with eclipses marked by grey shaded regions; the horizontal axis in the inset plots is in days since the start of the depicted observation. Note that the scaling between the PCA, XIS0, and ISGRI light curves is arbitrary.

off-source positions to obtain near-real-time background data; while there were times later in the mission where this rocking mechanism failed, all *RXTE* observations of 4U 1538−522 were taken while both HEXTE rocking mechanisms were functional.

Four *RXTE* proposals included observations of 4U 1538−522: P10145, P20146, P50067, and P80016. P20146 was a monitoring campaign: a year's worth of monthly snapshot observations between 1996 and 1997, each with ∼2 ks exposure, The remaining three proposals, from 1997, 2001, and 2003, respectively, were dedicated pointed observations with many observations within a few 3.7 d orbital periods. Each proposal's data are divided into multiple observation IDs with exposures ranging from a few to a few dozen kiloseconds each; after excluding observations taken close to and during the X-ray eclipse, our final *RXTE* data set comprises 50 obsids. We extracted PCA and HEXTE spectra and light curves from each obsid using the standard *RXTE* pipeline found in version 6.16 of the HEASOFT software distribution. We then determined the pulse period of the source and extracted spectra in luminosity and phase bins of interest to this analysis.

Calibration uncertainties in the background modelling for the *RXTE* PCA at high energies can result in the background count rate being over- or underestimated by a few per cent. Thus, during spectral fitting, we correct the background in the PCA via the `corback` procedure in ISIS. The magnitude of this shift was typically of the order of a few per cent, on average reducing the background counting rate by ∼2 per cent. This correction allowed us to take PCA spectra between 3 and 60 keV; HEXTE spectra were used between 18 and 80 keV.

2.2 *Suzaku* data

Suzaku carries two sets of instruments: four X-ray Imaging Spectrometers (XIS 0-3; Koyama et al. 2007) and the Hard X-ray Detector (HXD; Takahashi et al. 2007). The XIS telescopes are imaging CCD detectors with 0.2–12 keV energy ranges. XIS2 was taken offline in 2006 after a micrometeorite impact, and so we only use XIS0, XIS1, and XIS3 data. The HXD consists of a set of silicon PIN diodes (energy range 10–70 keV) and a GSO scintillator

(40–600 keV); we only used HXD/PIN data in the hard X-ray band, as the GSO signal-to-noise ratio was very low.

Suzaku observed 4U 1538−522 on 2012 August 10 for 61.9 ks. The reduction of the *Suzaku* data is explained at length in Hemphill et al. (2014). In this analysis, we focus on the phase-averaged data from the first half of the observation (as the second half contains significantly higher variability), as well as the pulse phase-constrained spectrum of the peak of the main pulse and the secondary pulse (phase bins 1 and 4 in Hemphill et al. 2014). The data were reprocessed and spectra were extracted using the standard *Suzaku* pipeline in HEASOFT v6.16. We used XIS data between 1 and 12 keV, taking the standard step of ignoring bins between 1.6 and 2.3 keV due to calibration uncertainties in that range. Data below 1 keV was ignored to avoid having to model the soft excess at those energies, which is outside the scope of this work. We rebinned the XIS spectra according to the binning scheme used by Nowak et al. (2012), which attempts to best account for the spectral resolution of the XIS detectors. The HXD/PIN data were used between 15 and 60 keV and rebinned to a minimum of 100 counts per bin.

2.3 *INTEGRAL* data

We used two of the instruments aboard *INTEGRAL* to supplement the *RXTE* and *Suzaku* analysis: the INTEGRAL Soft Gamma-Ray Imager (ISGRI), a 15 keV–2 MeV CdTe imager which forms the upper layer of the coded-mask IBIS telescope, and Joint European X-Ray Monitor (JEM-X), a pair of coded mask X-ray monitors which work in the 3–35 keV band. There are a total of 870 ∼2 ks exposure science windows (SCWs) which include 4U 1538−522 within the 9° × 9° fully coded field of view (FCFOV) of ISGRI and 211 with the source inside the 4.°8-diameter FCFOV of JEM-X. We extracted ISGRI and JEM-X spectra using the standard analysis pipelines found in version 10.0 of the Offline Scientific Analysis (OSA) software package.

The available data lie mostly in a few *INTEGRAL* revolutions, so we produced four spectra each for ISGRI and JEM-X 1, adding together SCWs from revolutions 0200 through 0299, 0300 through 0399, 0700 through 0799, and 0900 through 0999, totalling 667 ISGRI and 125 JEM-X 1 SCWs (there were not enough JEM-X 2 SCWs in this data set to produce good spectra). These cover the years 2004–2006 and 2009–2010. This extraction provides long exposures (long exposures are needed due to the low signal-to-noise inherent in coded-mask detectors) while still maintaining some time resolution.

The background for each pixel in a coded-mask detector contains contributions from every point on the sky in the field of view (FOV), so it was necessary to compile a list of bright sources in the FOV for each SCW. This list was fed back into the background subtraction routines in the standard spectral extraction procedure. These data give us *INTEGRAL* results that lie in the temporal gap between the *RXTE* and *Suzaku* observations. Several *INTEGRAL* revolutions from after 2010 include many SCWs with 4U 1538−522 in the FOV; however, these data are rather sparse and, due to the long-term evolution of the ISGRI detector, the recommendation for the most recent observations is to ignore data below 22 keV.[2] For these reasons, these data are not suitable for this analysis.

[2] See version 10.0 of the IBIS Analysis User Manual.

Table 2. Orbital parameters of 4U 1538−522.

Parameter	Units	Mukherjee et al. (2006) value
$a \sin(i)$	lt-s	53.1 ± 1.5
e		0.18 ± 0.01
$P_{\rm orb}$	d	$3.728\,382 \pm 0.000\,011$
$T_{\pi/2}$	MJD	$52\,851.33 \pm 0.01$
$\omega_{\rm d}$		$40^\circ \pm 12^\circ$

Table 3. Pulse period measurements for 4U 1538−522 using *RXTE* and *Suzaku*.

Obs.	MJD range	Pulse period (s)	$\dot{P}$ (10^{-10} s s^{-1})
P10145	50450.62–50453.67	528.824 ± 0.014	
P20146	50411.96–50795.17	$527.9775^{+0.0014}_{-0.0006}$	-5.9 ± 0.3
P50067	51924.62–51928.56	527.596 ± 0.009	
P80016	52851.96–52858.38	526.834 ± 0.009	
Suzaku [a]	56149.02–56149.73	525.59 ± 0.04	

Note. [a]from Hemphill et al. (2014).

3 TIMING ANALYSIS

To determine the pulse period of the source, we extracted barycentred light curves for each *RXTE* obsid. After applying a binary orbit correction using orbital parameters from Clark (2000) and Mukherjee et al. (2006) (see Table 2), we used epoch folding (Leahy et al. 1983) to determine an initial guess for the pulse period in each obsid. By folding the light curve on the pulse period, we produced a 'reference' pulse profile for each obsid, which was then compared via cross-correlation to each individual pulse in the light curve (the source is bright enough that individual pulses are clearly visible in the *RXTE*/PCA light curve, so no averaging was necessary). The peak in the cross-correlation results gives the phase shift between the reference pulse profile and the individual pulse. By fitting the time-of-arrival and phase-shift results for each *RXTE* proposal with a polynomial in pulse frequency, a more precise picture of the pulse period can be obtained, as a linear trend in the phase shift over time indicates a shift in the frequency from the originally assumed value, while higher order terms in the fit return the derivatives of the pulse frequency

$$\delta\varphi(t) = \varphi_0 + \delta\nu(t - t_0) + \frac{1}{2}\dot{\nu}(t - t_0)^2. \quad (1)$$

Here, t contains the times-of-arrival of the pulses, φ_0 is the phase at $t = t_0$ (in our case, we define φ_0 and t_0 such that the peak of the main pulse is $\varphi = 0.0$), $\delta\nu$ is the deviation of the true pulse frequency from the originally assumed value computed by epoch folding, and $\dot{\nu}$ is the pulse frequency derivative. With the exception of *RXTE* proposal P20146, the *RXTE* data were over short enough timespans that the evolution of the pulse period was not needed in the model, and we fixed $\dot{\nu}$ to zero in these cases. This returns results which are broadly in line with the analyses of Coburn (2001) and Baykal et al. (2006). Our pulse period measurements, with 90 per cent confidence intervals, are displayed in Table 3. We additionally include the pulse period during the *Suzaku* observation, as reported in Hemphill et al. (2014).

In Fig. 2, we plot the 2–10 and 20–30 keV pulse profiles for the three focused *RXTE* proposals (P10145, P50067, and P80016) using PCA as well as the *Suzaku* observation (using the XIS for the 2–10 keV profile and the PIN for the 20–30 keV profile), with the phase bins used in our spectral extraction indicated. Due

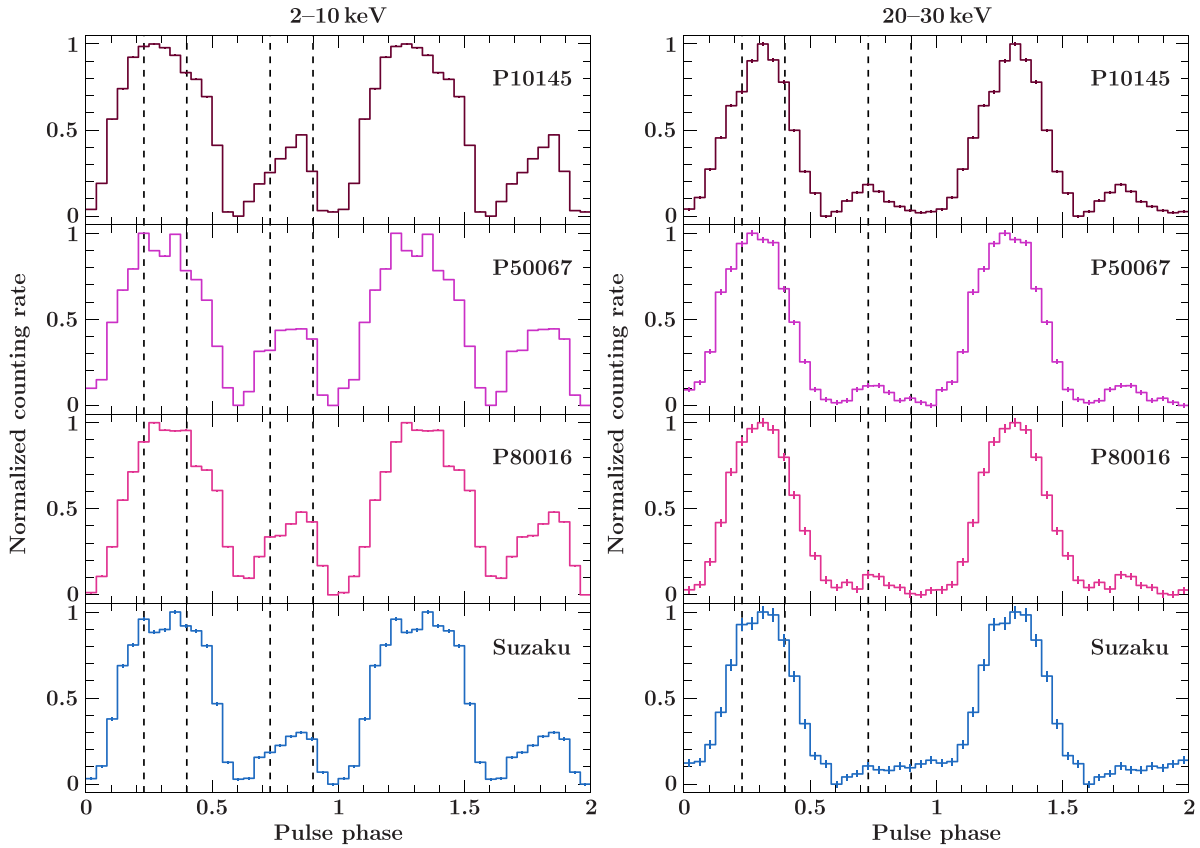

Figure 2. Left-hand panels: the 2–10 keV pulse profiles using *RXTE*-PCA and *Suzaku*-XIS. Right-hand panels: 20–30 keV pulse profiles using *RXTE*-PCA and *Suzaku*-HXD/PIN. The *RXTE* proposal ID for each PCA profile is indicated. Profiles were obtained by folding the respective light curve on the pulse periods from Table 3. The phase intervals for pulse-phase-constrained spectral extraction are indicated by dashed lines.

to the long timespan and relatively large uncertainty in $\dot{P}$ for *RXTE* proposal P20146, we do not plot the profile for that set of obsids. At higher energies, the primary pulse narrows and the secondary pulse weakens considerably; the pulse profiles for *RXTE* and *Suzaku* are qualitatively similar in both bands with the exception that the secondary pulse appears to vanish completely in the PIN profile, while the PCA profile still shows a weak secondary pulse. There are no pronounced phase shifts in the positions of the peaks or major changes in the overall structure of the pulse profile with energy, unlike, e.g. 4U 0115+63 (Ferrigno et al. 2009) or Vela X-1 (Kreykenbohm et al. 2002).

4 SPECTRAL ANALYSIS

Our aim in this paper is to examine and quantify the change over time in the CRSF energy of 4U 1538−522. This necessitates controlling for other parameters which may influence the measured line energy. Thus, we perform our analysis on four different selections of data. The first, and simplest, selection is the spectra from each of the *RXTE* obsids. This is a phase-averaged data set, with no cuts based on luminosity or pulse phase, although we do exclude observations taken during the eclipse. This data set comprises 50 *RXTE* spectra and the single *Suzaku* observation, and covers a fairly wide range of fluxes. Secondly, we determined the peak PCU2 counting rate in each individual pulse and produced a set of good time intervals (GTIs) for four counting rate bins, with cuts at 103, 123, 140, and 171 count s^{-1} (the *Suzaku* observation's mean flux is approximately in line with the 123–140 count s^{-1} *RXTE* bin). These GTIs were used to extract a set of phase-averaged and luminosity-selected spectra. Note that this data set is constructed on a pulse-by-pulse basis, adding up all individual pulses in a proposal that are in a given range of counting rates. This avoids averaging over too broad of a range of fluxes while also ensuring that the data set is fully phase-averaged, with better statistics than the obsid-by-obsid data set. Finally, using the pulse period of the source, we produced GTIs and extracted spectra for the peak of the main pulse and for the secondary pulse.

For our pulse-phase-constrained analysis, in order to ensure that we selected the same pulse phase bins across all data sets, we computed the cross-correlation between the 2–10 keV *RXTE* PCA and *Suzaku* XIS profiles; the shift in the PCA profile which gives the largest value of the correlation coefficient is thus the phase shift between that PCA profile and the XIS profile, which was then used to define phase 0.0 in all data sets. For *RXTE* proposals P10145, P50067, and P80016, we used the pulse profile from the full proposal light curve, as the change in the pulse period is small over the few days that each proposal spans. *RXTE* proposal P20146 was treated on an obsid-by-obsid basis due to its extended duration and the long gaps between observations. The pulse phase bins used for the *RXTE* data thus correspond to the first and fourth phase bins used in Hemphill et al. (2014), each of which has a width of one-sixth of the pulse. The phase bins used are plotted in Fig. 2.

The main pulse spectra were restricted to a PCA counting rate between 60 and 200 count s^{-1} and the secondary pulse spectra were restricted to a 50–160 count s^{-1} range in order to avoid major dips and flares. This phase-resolved analysis is essential, as the

CRSF energy varies over 4U 1538−522's pulse by 5–10 per cent (1–2 keV; Hemphill et al. 2014). Since the phase-averaged CRSF energy is the weighted average of the observed CRSF across all phase bins, any long-term evolution in either the pulse shape or the CRSF's variability with pulse phase could potentially influence the measured CRSF energy in phase-averaged spectra. Performing this pulse phase-constrained analysis allows us to account for this effect.

For *Suzaku*, we produced a single set of XIS and HXD/PIN spectra for the first half of the observation (this is effectively the sum of phase-averaged spectra 1 through 4 in Hemphill et al. 2014) for comparison to the phase-averaged and luminosity-resolved *RXTE* spectra, while for comparison to the pulse-phase-constrained *RXTE* spectra we took the corresponding bins (phase-resolved spectra 1 and 4) from the phase-resolved spectra of Hemphill et al. (2014). The quality of the *INTEGRAL* data is not high enough to warrant phase-resolved spectroscopy, so we simply use the four sets of phase-averaged spectra as described in Section 2.3 for comparison to the phase-averaged *RXTE* and *Suzaku* data sets.

4.1 Spectral model

The choice of spectral model can influence the measured CRSF parameters (see e.g. Müller et al. 2013a). Thus, an important first step is to ensure that every spectrum is fit with the same model. There are several different phenomenological continuum models used for accreting X-ray pulsars, and while no model is devoid of problems, the model that we found worked best overall for *RXTE*, *Suzaku*, and *INTEGRAL* was a power-law of photon index Γ modified by the standard `highecut` high-energy cutoff (White, Swank & Holt 1983):

$$\texttt{plcut}(E) = \begin{cases} AE^{-\Gamma} & E < E_{\rm cut} \\ AE^{-\Gamma} \exp\left(\frac{E_{\rm cut}-E}{E_{\rm fold}}\right) & E \geq E_{\rm cut} \end{cases}. \quad (2)$$

This piecewise model can result in spurious features around the cutoff energy $E_{\rm cut}$; we account for this by including a narrow (width frozen to 0.01 keV) negative Gaussian with its energy tied to the cutoff energy $E_{\rm cut}$ (see e.g. Coburn et al. 2002; Fürst et al. 2013). For simplicity, we will refer to this modified power-law cutoff continuum model as `mplcut`.

The CRSF at ∼21 keV is modelled using a Gaussian optical depth profile, `gauabs`. This model component is identical to the XSPEC model `gabs` with a slightly different definition of the line depth parameter, which here represents the maximum optical depth in the line, τ_0:

$$\texttt{gauabs}(E) = e^{-\tau(E)} \quad (3)$$

$$\tau(E) = \tau_0 \exp\left(-\frac{(E-E_0)^2}{2\sigma^2}\right). \quad (4)$$

The first harmonic of the CRSF is at ∼50 keV in 4U 1538−522 (Rodes-Roca et al. 2009; Hemphill et al. 2013). We include the harmonic CRSF in the phase-averaged, luminosity-selected spectra, using a `gauabs` feature with its depth free to vary but with energy and width fixed to 50 and 5 keV, respectively. The feature is only detected (i.e. depth inconsistent with zero) in the brightest spectra, but we include it in all the phase-averaged spectra in order to ensure consistency in this data set. The harmonic CRSF was not detected in the individual obsids or the pulse phase-constrained data and thus was not included in the final model for those data sets. We performed fits for *Suzaku* with and without the harmonic CRSF, but the only noticeable effect on the fitted parameters was a slight decrease in the source flux (due mainly to our chosen energy range of 3–50 keV including part of the harmonic CRSF).

Several X-ray pulsars, 4U 1538−522 included, show a peculiar feature in their ∼8–12 keV spectrum. This typically appears as broad emission around ∼10–11 keV (as such, it is usually called the '10-keV bump' or '10-keV feature'), although it can be modelled as an absorption feature at somewhat lower energy (Müller et al. 2012). A discussion of this feature, along with several examples, can be found in Coburn (2001), although currently no satisfactory physical explanation exists. In this work, most (∼80 per cent) of our spectra were poorly fit without a 10-keV feature, with reduced $\chi^2 > 1.4$. In these poorly fitted cases, we include a `gauabs` feature in the model with energy ∼8.5 keV and width frozen to 1 keV. However, in the ∼20 per cent of spectra which were well fitted without such a feature, its inclusion tended to severely overfit the spectrum (reduced $\chi^2 \lesssim 0.5$). We thus include the feature only in the poorly fit cases, in order to bring the reduced χ^2 down to ∼1 and obtain realistic error bars on the other fitted parameters. There do not seem to be any systematic factors which determine whether or not a particular spectrum will need an 8-keV dip; the distributions of fitted parameters and uncertainties for spectra with and without 8-keV features are entirely consistent with each other. However, spectra which did not need an 8-keV dip to obtain a good fit do tend to have lower total counts, with an average of 7.7×10^5 counts compared to 1.8×10^6 for the spectra with an 8-keV dip. Thus, the lack of an 8-keV dip in some spectra is an issue of data quality and is not of physical origin. We also tried fitting with an emissive feature at ∼11 keV as has been used before (Rodes-Roca et al. 2009; Hemphill et al. 2013); however, the broad width of the 10-keV feature led to it interfering with the parameters of the CRSF.

We do include an 8-keV dip in the model for *Suzaku*, in order to bring that model as close as possible to the one we used for *RXTE*. Its depth and energy are consistent with the values found by *RXTE*. The *INTEGRAL* spectra suffered from the same issues as the lower-quality *RXTE* spectra in this matter, so we did not include an 8-keV feature in those spectra.

The spectral model is further modified by an additive Gaussian emission line modelling the iron Kα at ∼6.4 keV, as well as photoelectric absorption, using the latest version[3] of the `tbnew` absorption model (Wilms et al. 2010). We used the abundances from Wilms, Allen & McCray (2000) and the cross-sections from Verner et al. (1996). The iron Kα energy is fixed to 6.4 keV in the *RXTE* spectra, and the line width is fixed to 0.01 keV in all spectra, as it is unresolved even at the energy resolution of *Suzaku*'s XIS.

To finish out the model, we apply a multiplicative constant to each instrument to account for flux calibration differences between the PCA and HEXTE, the XIS and HXD/PIN, and *INTEGRAL*'s JEM-X and ISGRI. The XIS0, PCA, and JEM-X constants were fixed to 1, while HEXTE and ISGRI's constants were allowed to vary, with the HEXTE constant typically taking values around ∼0.85 and ISGRI's constant being found between 0.8 and 1. For *Suzaku*, we left the HXD/PIN calibration constant free to vary in the phase-averaged data, finding a value of $1.02^{+0.08}_{-0.02}$. The phase-constrained spectra were very difficult to constrain with the calibration constant left free to vary, so we fixed it to the recommended value of 1.16 in that data set. We plot a representative *RXTE* spectral fit and the best-fitting *Suzaku* spectrum and model in Fig. 3.

[3] See http://pulsar.sternwarte.uni-erlangen.de/wilms/research/tbabs/

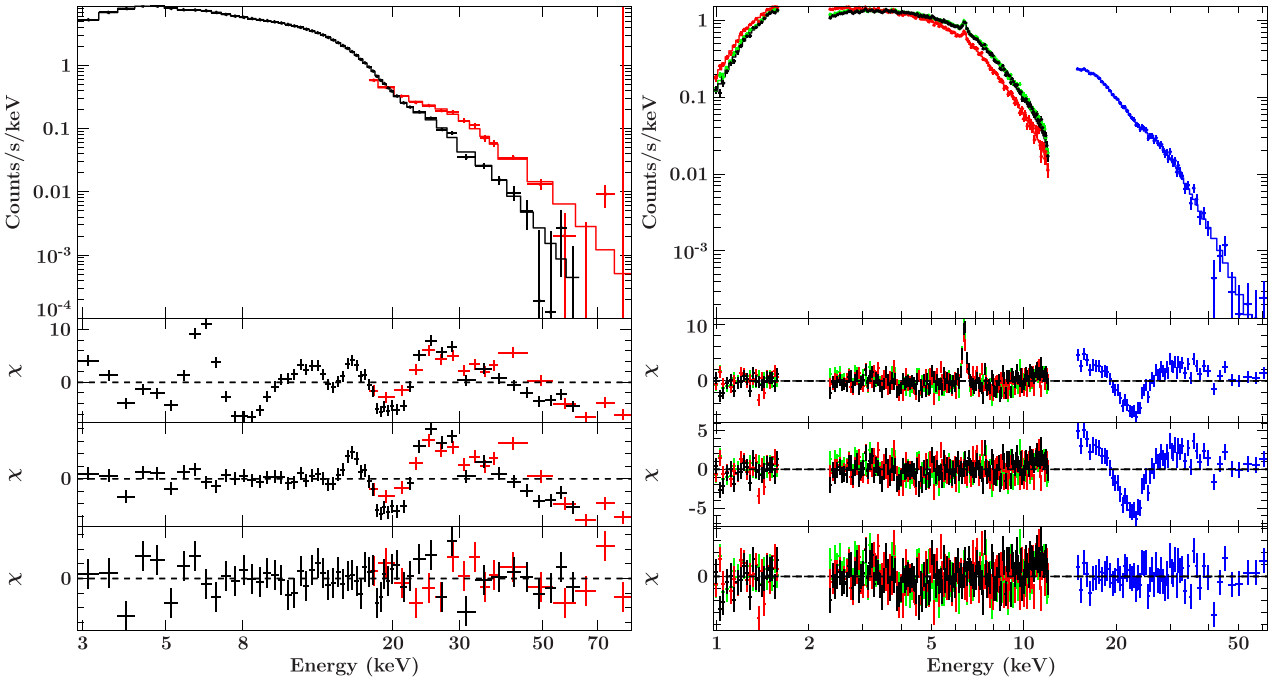

Figure 3. Representative phase-averaged *RXTE* (left-hand panel) and *Suzaku* (right-hand panel) spectra. The *RXTE* spectra are from proposal P50067 in the 140–171 count s^{-1} flux bin, with PCA plotted in black and HEXTE plotted in red. For *Suzaku*, XIS 0, 1, and 3 are plotted in black, red, and green, respectively, and the HXD/PIN is plotted in blue. In each plot, the top panel displays the counts spectrum with the best-fitting model overplotted, while the lower panels display, from top to bottom, the residuals for a fit with only a `mplcut` continuum, the `mplcut` continuum with a 6.4 keV iron Kα line and an 8-keV dip, and the best-fitting residuals including the CRSF.

As a check, we also performed fits with a continuum consisting of a powerlaw multiplied by a 'Fermi-Dirac' cutoff (Tanaka 1986):

$$\texttt{fdcut}(E) = AE^{-\Gamma} \times \left[1 + \exp\left(\frac{E - E_{\rm cut}}{E_{\rm fold}}\right)\right]^{-1}. \quad (5)$$

This, unlike `plcut`, is not piecewise. However, `fdcut` tended to fit the *RXTE* data worse than `mplcut`; while we were eventually able to obtain comparable goodness-of-fit to our `mplcut` results, it was necessary to include a significantly deeper 8-keV dip, with central optical depths greater by a factor of ∼2–10. In the cases with the most pronounced 8-keV dip, the remaining spectral parameters were very poorly constrained. Fitting with an emissive Gaussian at ∼11 keV resulted in somewhat better constraints on the continuum parameters, but lead to the same difficulty disentangling the CRSF and 10-keV bump as we encountered using `mplcut`. Thus, we will rely primarily on our `mplcut` results, supplementing with the `fdcut` results when applicable.

In all cases, we calculate the unabsorbed continuum flux in the 3–50 keV band by convolving our continuum model, 8-keV dip, and CRSFs with an `enflux` spectral component in ISIS. We fit the *RXTE* and *Suzaku* spectra with this model (omitting the harmonic CRSF in the case of the individual *RXTE* obsids), and calculated 90 per cent error bars on all parameters. We used a considerably simpler model for the *INTEGRAL* spectra, omitting the absorption, iron line, and 8-keV dip – the low spectral sensitivity and 5 keV lower energy bound of JEM-X meant these features were undetected.

5 RESULTS

Our analysis finds that 4U 1538−522 displays few significant correlations between spectral parameters. The spectral shape is relatively stable over time, although the parameters are often quite broadly scattered, especially in the obsid-by-obsid data set. We present the spectral parameters for the pulse-by-pulse, phase-averaged *RXTE* data set in Table 4, and the parameters for the pulse-phase-constrained data sets in Table 5. The *Suzaku* and *INTEGRAL* parameters are presented in Tables 6 and 7, respectively. It was necessary in a few cases to freeze spectral parameters to obtain a stable fit: the 3 keV lower energy bound of the *RXTE*/PCA meant we had to freeze $N_{\rm H}$ to its fitted value in the 123–140 count s^{-1} bin of proposal P10145 and the 140–171 count s^{-1} bin of proposal 80016. Both spectra found $N_{\rm H}$ at 2.9×10^{22} cm^{-2}; since this low of an $N_{\rm H}$ does not have strong effects on the spectrum above 3 keV, it is unlikely that fixing this parameter has large effects on the other parameters. We also froze the energy of the 8-keV dip to 8.5 keV in the model for the secondary pulse in both *RXTE* and *Suzaku* due to the relatively poor quality and low flux of those spectra. Finally, it was necessary to freeze both the photon index to 1.2 and the CRSF width to 3 keV in the *INTEGRAL* spectra from the 900–999 revolutions to obtain a stable fit.

We plot the iron line flux, photon index, absorbing column density, and 8-keV feature depth against luminosity (calculated from the unabsorbed 5–50 keV flux) in Fig. 4. The iron line flux shows a clear positive correlation with luminosity, with a slope of $(0.93 \pm 0.03) \times 10^{-3}$ ph cm^{-2} s^{-1} per 10^{37} erg s^{-1} in the obsid-by-obsid data set, while the photon index Γ displays a negative correlation with luminosity, with a linear fit finding a slope of -0.262 ± 0.006 in the obsid-by-obsid data set. In both of these cases, the fitted slope in the pulse-by-pulse data set is highly consistent with the obsid-by-obsid result; the positive correlation between the iron line flux and broad-band flux is not seen in the pulse-phase-constrained results, but the iron line is near its weakest flux in the pulse peak (Hemphill et al. 2014) and the secondary peak phase bin has low flux overall, making the iron line difficult to

Table 4. Pulse-by-pulse spectral parameters from *RXTE*, with 90 per cent confidence intervals.

	PCU2 counting rate bin	171–575	140–171	123–140	103–123
RXTE proposal P10145					
3–50 keV flux	10^{-9} erg cm^{-2} s^{-1}	$1.884^{+0.027}_{-0.026}$	$1.060^{+0.022}_{-0.015}$	0.927 ± 0.019	$0.766^{+0.019}_{-0.011}$
$N_{\rm H}$	10^{22} cm^{-2}	1.65 ± 0.30	1.8 ± 0.4	2.9 (frozen)	4.5 ± 0.4
Γ		$1.047^{+0.016}_{-0.015}$	$1.079^{+0.019}_{-0.011}$	$1.1571^{+0.0073}_{-0.0020}$	$1.176^{+0.014}_{-0.000}$
$E_{\rm cut}$	keV	14.1 ± 0.4	$14.9^{+0.5}_{-0.4}$	$14.7^{+0.5}_{-1.4}$	$14.5^{+0.4}_{-0.7}$
$E_{\rm fold}$	keV	$11.3^{+0.6}_{-0.5}$	$10.1^{+0.8}_{-0.5}$	11.3 ± 0.9	$11.00^{+1.19}_{-0.23}$
$A_{\rm smooth}$	10^{-3} ph cm^{-2} s^{-1}	$5.4^{+1.4}_{-1.6}$	$4.7^{+1.8}_{-1.9}$	<4.9	$3.2^{+1.4}_{-1.7}$
$E_{\rm cyc}$	keV	$20.78^{+0.25}_{-0.24}$	20.8 ± 0.4	$20.67^{+0.29}_{-0.12}$	$20.492^{+0.307}_{-0.024}$
$\sigma_{\rm cyc}$	keV	$2.79^{+0.26}_{-0.19}$	$2.94^{+0.30}_{-0.25}$	$2.64^{+0.17}_{-0.76}$	$2.42^{+0.22}_{-0.42}$
$\tau_{\rm cyc}$		0.45 ± 0.04	0.55 ± 0.06	$0.548^{+0.018}_{-0.090}$	$0.531^{+0.019}_{-0.070}$
$\tau_{\rm harm}$		$1.2^{+1.0}_{-0.6}$	<2.8	<0.9	<1.2
$A_{\rm Fe}$	10^{-3} ph cm^{-2} s^{-1}	0.76 ± 0.12	$0.28^{+0.09}_{-0.08}$	0.32 ± 0.07	0.29 ± 0.07
$E_{\rm dip}$	keV		$8.45^{+0.29}_{-0.34}$	8.5 ± 0.4	$8.83^{+0.22}_{-0.23}$
$\tau_{\rm dip}$			$0.045^{+0.013}_{-0.011}$	$0.039^{+0.011}_{-0.010}$	0.063 ± 0.012
HEXTE constant		0.803 ± 0.017	0.768 ± 0.025	$0.765^{+0.024}_{-0.023}$	0.79 ± 0.04
$\chi^2_{\rm red}$ (dof)		1.28 (65)	1.22 (63)	1.34 (64)	0.96 (63)
RXTE proposal P20146					
3–50 keV flux	10^{-9} erg cm^{-2} s^{-1}	1.45 ± 0.04	$1.108^{+0.018}_{-0.013}$	$0.884^{+0.032}_{-0.030}$	$0.731^{+0.030}_{-0.026}$
$N_{\rm H}$	10^{22} cm^{-2}	2.1 ± 0.4	$2.49^{+0.30}_{-0.36}$	1.9 ± 0.5	3.4 ± 0.5
Γ		1.104 ± 0.019	$1.115^{+0.023}_{-0.018}$	$1.172^{+0.023}_{-0.000}$	$1.192^{+0.023}_{-0.026}$
$E_{\rm cut}$	keV	$13.55^{+0.50}_{-0.25}$	$14.9^{+0.6}_{-1.7}$	$13.90^{+0.59}_{-0.30}$	$14.0^{+1.2}_{-0.9}$
$E_{\rm fold}$	keV	$11.9^{+1.0}_{-0.9}$	$10.5^{+1.4}_{-0.5}$	$11.0^{+1.6}_{-1.4}$	$11.4^{+1.9}_{-2.0}$
$A_{\rm smooth}$	10^{-3} ph cm^{-2} s^{-1}	<2.1	3.7 ± 1.7	<1.5	<5.8
$E_{\rm cyc}$	keV	20.7 ± 0.4	$20.68^{+0.34}_{-0.30}$	21.0 ± 0.6	$20.3^{+0.6}_{-0.8}$
$\sigma_{\rm cyc}$	keV	2.2 ± 0.4	$2.9^{+0.4}_{-1.0}$	2.3 ± 0.6	$2.3^{+0.8}_{-0.9}$
$\tau_{\rm cyc}$		0.46 ± 0.06	$0.54^{+0.07}_{-0.12}$	0.46 ± 0.10	$0.43^{+0.08}_{-0.10}$
$\tau_{\rm harm}$		<0.5	<1.0	<2.0	<5.0
$A_{\rm Fe}$	10^{-3} ph cm^{-2} s^{-1}	0.56 ± 0.12	$0.39^{+0.08}_{-0.09}$	0.41 ± 0.09	0.27 ± 0.07
$E_{\rm dip}$	keV		$8.45^{+0.31}_{-0.28}$		$8.9^{+0.4}_{-0.5}$
$\tau_{\rm dip}$			$0.042^{+0.013}_{-0.009}$		$0.057^{+0.017}_{-0.015}$
HEXTE constant		$0.777^{+0.027}_{-0.026}$	0.792 ± 0.022	0.80 ± 0.05	0.81 ± 0.05
$\chi^2_{\rm red}$ (dof)		0.86 (65)	1.07 (63)	1.29 (65)	1.00 (63)
RXTE proposal P50067					
3–50 keV flux	10^{-9} erg cm^{-2} s^{-1}	$1.844^{+0.016}_{-0.013}$	1.219 ± 0.016	$1.002^{+0.017}_{-0.016}$	$0.927^{+0.021}_{-0.019}$
$N_{\rm H}$	10^{22} cm^{-2}	$2.68^{+0.30}_{-0.25}$	$3.00^{+0.33}_{-0.24}$	$4.6^{+0.4}_{-0.5}$	$6.8^{+0.6}_{-0.5}$
Γ		$1.045^{+0.018}_{-0.016}$	$1.119^{+0.017}_{-0.016}$	$1.105^{+0.016}_{-0.017}$	$1.020^{+0.015}_{-0.006}$
$E_{\rm cut}$	keV	$15.12^{+0.39}_{-0.28}$	$14.3^{+0.4}_{-0.6}$	$13.63^{+0.25}_{-0.19}$	$14.5^{+0.4}_{-1.2}$
$E_{\rm fold}$	keV	10.1 ± 0.4	$11.2^{+0.6}_{-0.5}$	10.6 ± 0.6	$10.3^{+0.9}_{-0.6}$
$A_{\rm smooth}$	10^{-3} ph cm^{-2} s^{-1}	$4.4^{+0.5}_{-1.4}$	$2.7^{+1.1}_{-1.4}$	$4.3^{+3.6}_{-2.9}$	$5.4^{+2.3}_{-3.9}$
$E_{\rm cyc}$	keV	$20.69^{+0.18}_{-0.16}$	$20.77^{+0.22}_{-0.20}$	$20.88^{+0.26}_{-0.25}$	$20.92^{+0.33}_{-0.10}$
$\sigma_{\rm cyc}$	keV	$3.47^{+0.24}_{-0.17}$	$2.84^{+0.23}_{-0.35}$	$2.28^{+0.33}_{-0.27}$	$2.92^{+0.16}_{-0.61}$
$\tau_{\rm cyc}$		$0.516^{+0.013}_{-0.023}$	$0.52^{+0.04}_{-0.05}$	0.47 ± 0.05	$0.62^{+0.06}_{-0.08}$
$\tau_{\rm harm}$		$0.7^{+0.5}_{-0.4}$	<0.6	<1.3	<0.8
$A_{\rm Fe}$	10^{-3} ph cm^{-2} s^{-1}	$0.84^{+0.13}_{-0.12}$	$0.47^{+0.10}_{-0.08}$	0.38 ± 0.07	0.32 ± 0.09
$E_{\rm dip}$	keV	$8.4^{+0.4}_{-0.5}$	$8.30^{+0.26}_{-0.33}$	$8.31^{+0.24}_{-0.27}$	$8.96^{+0.29}_{-0.33}$
$\tau_{\rm dip}$		$0.026^{+0.015}_{-0.009}$	$0.043^{+0.009}_{-0.010}$	0.044 ± 0.008	0.052 ± 0.014
HEXTE constant		$0.797^{+0.010}_{-0.008}$	0.805 ± 0.016	$0.836^{+0.022}_{-0.021}$	0.803 ± 0.027
$\chi^2_{\rm red}$ (dof)		1.83 (58)	1.29 (58)	1.01 (57)	0.97 (58)

Table 4 – *continued*

	PCU2 counting rate bin	171–575	140–171	123–140	103–123
RXTE proposal P80016					
3–50 keV flux	10^{-9} erg cm^{-2} s^{-1}	1.818 ± 0.027	1.271 ± 0.029	$1.016^{+0.029}_{-0.028}$	0.874 ± 0.017
$N_{\rm H}$	10^{22} cm^{-2}	3.3 ± 0.5	2.9 (frozen)	6.3 ± 0.7	4.7 ± 0.5
Γ		$1.007^{+0.022}_{-0.021}$	$1.043^{+0.015}_{-0.027}$	1.05 ± 0.04	1.085 ± 0.022
$E_{\rm cut}$	keV	$14.3^{+0.5}_{-0.4}$	$13.2^{+7.7}_{-0.5}$	$13.8^{+1.0}_{-0.5}$	$13.9^{+0.6}_{-0.4}$
$E_{\rm fold}$	keV	$11.6^{+0.6}_{-0.4}$	$12.7^{+1.1}_{-3.1}$	11.8 ± 1.1	10.7 ± 0.8
$A_{\rm smooth}$	10^{-3} ph cm^{-2} s^{-1}	$6.1^{+2.2}_{-1.2}$	<3.6	<4.0	<2.6
$E_{\rm cyc}$	keV	$20.76^{+0.31}_{-0.30}$	$20.9^{+0.5}_{-0.6}$	21.1 ± 0.5	20.8 ± 0.4
$\sigma_{\rm cyc}$	keV	$3.04^{+0.30}_{-0.25}$	$2.7^{+0.9}_{-0.5}$	2.8 ± 0.5	2.6 ± 0.4
$\tau_{\rm cyc}$		$0.451^{+0.030}_{-0.017}$	$0.45^{+0.23}_{-0.06}$	0.48 ± 0.08	0.51 ± 0.06
$\tau_{\rm harm}$		$1.5^{+1.1}_{-0.7}$	$2.1^{+2.7}_{-1.3}$	<1.9	<5.0
$A_{\rm Fe}$	10^{-3} ph cm^{-2} s^{-1}	0.59 ± 0.15	$0.38^{+0.14}_{-0.13}$	0.43 ± 0.12	0.37 ± 0.08
$E_{\rm dip}$	keV		$8.6^{+0.7}_{-1.1}$		
$\tau_{\rm dip}$			$0.029^{+0.019}_{-0.017}$		
HEXTE constant		0.778 ± 0.020	0.762 ± 0.029	0.83 ± 0.04	0.770 ± 0.026
$\chi^2_{\rm red}$ (dof)		0.87 (61)	1.28 (60)	1.25 (61)	1.37 (61)

constrain in PCA data in both phase-constrained data sets. Fits using the `fdcut` continuum find statistically similar results for these parameters.

The absorbing column density $N_{\rm H}$ varies over the binary orbit, typically sitting between 1 and 5×10^{22} cm^{-2} at most orbital phases, but rising dramatically to $\sim 10^{23}$ cm^{-2} near eclipse. We plot $N_{\rm H}$ versus orbital phase, using results from the obsid-by-obsid data set, in Fig. 5. While the increase in $N_{\rm H}$ near eclipse is primarily a line-of-sight effect, the high variability seen while the source is out of eclipse indicates highly variable local absorption, consistent with a clumpy or otherwise inhomogeneous stellar wind. Our observed variability in $N_{\rm H}$ is largely consistent with *RXTE*/PCA and *BeppoSAX* data analysed by Mukherjee et al. (2006) and with *MAXI* results from Rodes-Roca et al. (2015). Qualitatively, we see somewhat higher variability over the orbit compared to the *RXTE*/PCA results of Mukherjee et al. (2006), although this may be due to the different absorption model and abundances that we use compared to that analysis, in addition to our considerably larger energy coverage. $N_{\rm H}$ also appears to show some anticorrelation with the unabsorbed flux (see Fig. 4), but this correlation is statistically insignificant – taking $N_{\rm H}$ measurements from obsids between orbital phases 0.2 and 0.7 (i.e. ignoring eclipse ingress and egress), Pearson's r for these two parameters is −0.12, for a p-value of 0.52. The lowest observed $N_{\rm H}$ is $\sim 0.6 \times 10^{22}$ cm^{-2} and most obsids find $N_{\rm H}$ above 1×10^{22} cm^{-2}, consistent with the approximate line-of-sight Galactic $N_{\rm H}$ (Dickey & Lockman 1990; Kalberla et al. 2005; Willingale et al. 2013).[4] This would point towards the *local* absorption dropping to effectively undetectable levels at times – e.g. at those points we are viewing the NS through a 'hole' in the surrounding medium.

The energy of the 8-keV dip feature is uncorrelated with the source flux, with an average energy of 7.6 ± 1.6 keV in the pulse-by-pulse data set. However, the feature's depth is clearly inversely correlated with luminosity (Fig. 4), trending down by -0.057 ± 0.015 per 10^{37} erg s^{-1}. This decrease is in line with the fact that the brighter spectra tend to be less likely to need the feature at all, although with no physical explanation for the feature in the first place, the reason for the trend is unclear.

Across all *RXTE* obsids and the *INTEGRAL* and *Suzaku* measurements, the flux varies by a factor of ∼3, with most of the observations lying between 6 and 14×10^{-10} erg cm^{-2} s^{-1} (assuming a distance of 6.4 kpc, this translates to a luminosity between 3 and 7×10^{36} erg s^{-1}), reaching a peak luminosity of $\sim 1.2 \times 10^{37}$ erg s^{-1} during flares.

5.1 CRSF variability with luminosity

Previous analyses (Hemphill et al. 2013, 2014) have found only tentative evidence for correlations between 4U 1538−522's CRSF energy and luminosity. With our considerably larger data set, we can report the best limits yet on any correlation between these two parameters.

We plot the obsid-by-obsid and pulse-by-pulse CRSF energy versus the unabsorbed 3–50 keV flux in the left-hand panels of Fig. 6. Linear fits to the obsid-by-obsid and pulse-by-pulse *RXTE* data sets find slopes of -0.48 ± 0.13 and 0.11 ± 0.19 keV per 10^{37} erg s^{-1}, respectively. No trend is visible in the *RXTE* peak-pulse and secondary-pulse phase-constrained results (with the exception of the significantly higher-energy *Suzaku* measurement), consistent with what is seen in the pulse-by-pulse results.

The obsid-by-obsid results have an intriguing hint of a change in slope at a luminosity of $\sim 6 \times 10^{36}$ erg s^{-1}, with a slope of $+1.0 \pm 0.4$ keV per 10^{37} erg s^{-1} below this luminosity and -1.48 ± 0.35 keV per 10^{37} erg s^{-1} for higher luminosities. This is especially interesting given the observed bimodality of $E_{\rm cyc}$-luminosity slopes across all CRSF sources, with lower luminosity sources showing positive slopes and higher luminosity sources showing negative slopes. However, the obsids each average over a range of luminosities; the overall flatness of the pulse-by-pulse measurements may be a more authentic representation of the source's true behaviour. Breaking the pulse-by-pulse CRSF measurements at a luminosity of 6×10^{36} erg s^{-1} as we did for the obsid-by-obsid results, the slopes are -0.1 ± 0.8 and $+1.20 \pm 0.65$ keV per 10^{-37} erg s^{-1} for high and low luminosities, respectively. The upward trend at lower luminosities for this data

[4] As calculated by https://heasarc.gsfc.nasa.gov/cgi-bin/Tools/w3nh/w3nh.pl

Table 5. Phase-constrained spectral parameters for *RXTE*, with 90 per cent confidence intervals.

RXTE proposal P10145		Main pulse	Secondary pulse
3–50 keV flux	10^{-9} erg cm^{-2} s^{-1}	$1.459^{+0.021}_{-0.007}$	$0.701^{+0.014}_{-0.004}$
$N_{\rm H}$	10^{22} cm^{-2}	2.6 ± 0.4	3.2 ± 0.4
Γ		$0.881^{+0.015}_{-0.026}$	$0.9422^{+0.0016}_{-0.0009}$
$E_{\rm cut}$	keV	$14.6^{+0.7}_{-0.8}$	$19.6^{+0.5}_{-0.4}$
$E_{\rm fold}$	keV	$11.0^{+0.6}_{-0.7}$	$4.68765^{+0.00005}_{-0.14214}$
$A_{\rm smooth}$	10^{-3} ph cm^{-2} s^{-1}	$0.17^{+0.08}_{-0.09}$	0.19 ± 0.07
$E_{\rm cyc}$	keV	$21.32^{+0.25}_{-0.29}$	$20.747^{+0.030}_{-0.036}$
$\sigma_{\rm cyc}$	keV	3.2 ± 0.5	$3.08^{+0.00}_{-0.07}$
$\tau_{\rm cyc}$		0.48 ± 0.06	$1.54^{+0.08}_{-0.06}$
$A_{\rm Fe}$	10^{-3} ph cm^{-2} s^{-1}	$0.27^{+0.08}_{-0.10}$	0.38 ± 0.06
$E_{\rm dip}$	keV	$8.42^{+0.24}_{-0.23}$	8.5 (frozen)
$\tau_{\rm dip}$		$0.054^{+0.014}_{-0.009}$	$0.063^{+0.013}_{-0.012}$
HEXTE constant		0.786 ± 0.015	0.75 ± 0.04
$\chi^2_{\rm red}$ (dof)		0.85 (64)	0.75 (65)
RXTE proposal P20146		Main pulse	Secondary pulse
3–50 keV flux	10^{-9} erg cm^{-2} s^{-1}	$0.993^{+0.018}_{-0.017}$	$0.948^{+0.014}_{-0.008}$
$N_{\rm H}$	10^{22} cm^{-2}	$2.31^{+0.29}_{-0.32}$	$2.64^{+0.31}_{-0.25}$
Γ		$1.124^{+0.015}_{-0.018}$	$1.122^{+0.019}_{-0.015}$
$E_{\rm cut}$	keV	$14.3^{+1.1}_{-0.8}$	$15.12^{+0.27}_{-0.80}$
$E_{\rm fold}$	keV	$11.0^{+0.9}_{-1.0}$	$10.6^{+0.8}_{-0.5}$
$A_{\rm smooth}$	10^{-3} ph cm^{-2} s^{-1}	<0.15	$0.14^{+0.04}_{-0.06}$
$E_{\rm cyc}$	keV	$20.73^{+0.29}_{-0.31}$	$20.76^{+0.26}_{-0.16}$
$\sigma_{\rm cyc}$	keV	$2.7^{+0.5}_{-0.6}$	$3.11^{+0.26}_{-0.34}$
$\tau_{\rm cyc}$		$0.48^{+0.09}_{-0.07}$	$0.56^{+0.05}_{-0.07}$
$A_{\rm Fe}$	10^{-3} ph cm^{-2} s^{-1}	0.36 ± 0.07	0.40 ± 0.06
$E_{\rm dip}$	keV	$8.57^{+0.22}_{-0.25}$	8.5 (frozen)
$\tau_{\rm dip}$		$0.050^{+0.012}_{-0.010}$	$0.049^{+0.009}_{-0.011}$
HEXTE constant		$0.790^{+0.018}_{-0.019}$	$0.835^{+0.017}_{-0.014}$
$\chi^2_{\rm red}$ (dof)		0.81 (64)	0.77 (65)
RXTE proposal P50067		Main pulse	Secondary pulse
3–50 keV flux	10^{-9} erg cm^{-2} s^{-1}	1.805 ± 0.018	$0.912^{+0.014}_{-0.013}$
$N_{\rm H}$	10^{22} cm^{-2}	2.7 ± 0.4	4.0 ± 0.5
Γ		$0.870^{+0.016}_{-0.018}$	$0.901^{+0.025}_{-0.026}$
$E_{\rm cut}$	keV	$13.79^{+1.18}_{-0.25}$	$17.0^{+0.5}_{-0.4}$
$E_{\rm fold}$	keV	$11.2^{+0.4}_{-0.8}$	5.6 ± 0.4
$A_{\rm smooth}$	10^{-3} ph cm^{-2} s^{-1}	<0.22	<0.025
$E_{\rm cyc}$	keV	$21.15^{+0.17}_{-0.20}$	20.35 ± 0.20
$\sigma_{\rm cyc}$	keV	$2.74^{+0.52}_{-0.23}$	$3.19^{+0.17}_{-0.16}$
$\tau_{\rm cyc}$		$0.429^{+0.078}_{-0.023}$	$1.29^{+0.09}_{-0.08}$
$A_{\rm Fe}$	10^{-3} ph cm^{-2} s^{-1}	0.36 ± 0.11	0.55 ± 0.08
$E_{\rm dip}$	keV	$8.33^{+0.23}_{-0.26}$	8.5 (frozen)
$\tau_{\rm dip}$		0.052 ± 0.009	0.046 ± 0.013
HEXTE constant		$0.813^{+0.012}_{-0.011}$	0.842 ± 0.025
$\chi^2_{\rm red}$ (dof)		0.96 (59)	1.28 (60)
RXTE proposal P80016		Main pulse	Secondary pulse
3–50 keV flux	10^{-9} erg cm^{-2} s^{-1}	1.444 ± 0.019	$0.769^{+0.016}_{-0.015}$
$N_{\rm H}$	10^{22} cm^{-2}	3.3 ± 0.5	3.2 ± 0.6
Γ		$0.846^{+0.028}_{-0.024}$	$0.894^{+0.030}_{-0.031}$
$E_{\rm cut}$	keV	$14.9^{+0.5}_{-1.5}$	$22.6^{+1.3}_{-3.8}$
$E_{\rm fold}$	keV	$10.5^{+1.1}_{-0.5}$	$4.0^{+1.6}_{-0.7}$
$A_{\rm smooth}$	10^{-3} ph cm^{-2} s^{-1}	<0.3	<0.04
$E_{\rm cyc}$	keV	$20.68^{+0.32}_{-0.23}$	$21.8^{+0.4}_{-1.0}$
$\sigma_{\rm cyc}$	keV	$3.15^{+0.28}_{-0.82}$	$3.46^{+0.23}_{-0.22}$
$\tau_{\rm cyc}$		$0.49^{+0.05}_{-0.10}$	$2.12^{+0.14}_{-0.51}$
$A_{\rm Fe}$	10^{-3} ph cm^{-2} s^{-1}	$0.38^{+0.14}_{-0.12}$	0.39 ± 0.09
$E_{\rm dip}$	keV	$8.0^{+0.4}_{-0.5}$	8.5 (frozen)
$\tau_{\rm dip}$		0.045 ± 0.011	0.061 ± 0.016
HEXTE constant		0.790 ± 0.016	0.80 ± 0.04
$\chi^2_{\rm red}$ (dof)		0.72 (60)	0.80 (61)

set is only significant at the $\sim 2\sigma$ level and is entirely due to the two lowest luminosity measurements; while this suggests a break, similar to that seen in the obsid-by-obsid data set, at $\sim 4 \times 10^{36}$ erg s^{-1}, the lack of measurements at very low luminosity makes this trend highly suspect.

5.2 CRSF variability with time

In the phase-averaged and main-pulse spectra, there is a jump of approximately 1.5 keV in the energy of the cyclotron line between the *RXTE* and *Suzaku* measurements, as can be seen in the right-hand panels of Fig. 6 and the left-hand panel of Fig. 7, where we plot the results from the pulse-phase-constrained data sets. This shift is seen in both the `mplcut` and `fdcut` results. However, as can be seen in the right-hand panel of Fig. 7, there is no significant increase in the CRSF energy in the phase-constrained spectra of the secondary pulse; while the poorly constrained *Suzaku* results for that phase bin are at least partially to blame here, there are some arguments that this may be a real effect. In Fig. 8, we plot a closer look at the data-to-model ratio residuals in the energy band around the CRSF when the CRSF is excluded from the model, using the same data as plotted in Fig. 3. The dip due to the CRSF in the *Suzaku* PIN data is visibly higher energy compared to the *RXTE* data.

While the *INTEGRAL* results help to fill in the gap between the *RXTE* and *Suzaku* results, their high uncertainties limit their usefulness for this analysis. The *RXTE* results taken on their own do not show any consistent trend with time; linear fits to the obsid-by-obsid and pulse-by-pulse results disagree, finding downward (-0.033 ± 0.009 keV yr^{-1}) and upward ($+0.034 \pm 0.015$ keV yr^{-1}) trends, respectively.

To better quantify the statistical significance of the *Suzaku* measurement, and to avoid making any assumptions about the underlying distribution of CRSF energy measurements, we took a Monte Carlo approach. We constructed simulated obsid-by-obsid data sets by varying each measured CRSF energy randomly according to its 1σ uncertainty. Each trial in this manner thus produced a set of 51 simulated CRSF energy measurements (50 *RXTE* points and one *Suzaku* point); we then computed the significance of the simulated *Suzaku* point compared to the mean and standard deviation of the simulated *RXTE* points. Performing 10^6 trials in this manner, the *Suzaku* point was found on average 4.6σ above the *RXTE* points, with a spread of 1.2σ.

To examine the possibility of systematic, instrumental differences in CRSF measurements between *RXTE* and *Suzaku*, either due to differences in energy calibration or due to the difference in energy coverage between the two satellites, we simulated *Suzaku* spectra for each of the obsid-by-obsid *RXTE* spectral models using the `fakeit` procedure in ISIS. The CRSF energy as measured in these simulated spectra was generally within the uncertainties of the *RXTE* measurements, finding a mean energy of 20.6 keV

Table 6. *Suzaku* spectral parameters, with 90 per cent confidence intervals.

Parameter	Units	Phase-averaged	Pulse peak	Secondary pulse
3–50 keV flux	10^{-9} erg cm^{-2} s^{-1}	$1.132^{+0.023}_{-0.051}$	$1.91^{+0.04}_{-0.05}$	0.787 ± 0.014
$N_{\rm H}$	10^{22} cm^{-2}	2.185 ± 0.023	1.96 ± 0.04	2.29 ± 0.06
Γ		1.148 ± 0.012	$0.839^{+0.024}_{-0.023}$	$0.890^{+0.027}_{-0.032}$
$E_{\rm cut}$	keV	18.6 ± 0.9	$14.7^{+6.5}_{-1.0}$	$12.3^{+14.3}_{-0.9}$
$E_{\rm fold}$	keV	$9.9^{+0.5}_{-0.4}$	$10.1^{+0.7}_{-3.3}$	$8.1^{+0.6}_{-0.5}$
$A_{\rm smooth}$	10^{-3} ph cm^{-2} s^{-1}	24^{+4}_{-19}	<1.9	<3.9
$E_{\rm cyc}$	keV	$22.7^{+0.6}_{-1.0}$	$23.0^{+0.9}_{-1.0}$	21.2 ± 0.6
$\sigma_{\rm cyc}$	keV	$2.07^{+0.13}_{-0.72}$	$2.5^{+1.5}_{-1.2}$	$2.6^{+1.7}_{-0.6}$
$\tau_{\rm cyc}$		$0.63^{+0.23}_{-0.09}$	$0.30^{+0.28}_{-0.08}$	$0.78^{+0.14}_{-0.15}$
$\tau_{\rm harm}$		<2.7		
$A_{\rm Fe}$	10^{-3} ph cm^{-2} s^{-1}	0.377 ± 0.028	0.34 ± 0.06	0.41 ± 0.05
$E_{\rm dip}$	keV	8.2 ± 0.4	7.8 ± 0.4	8.5 (frozen)
$\tau_{\rm dip}$	10^{-3} ph cm^{-2} s^{-1}	0.031 ± 0.014	0.072 ± 0.022	0.10 ± 0.04
$\chi^2_{\rm red}$ (dof)		1.25 (520)	1.17 (509)	1.04 (494)

Table 7. *INTEGRAL* spectral parameters, with 90 per cent confidence intervals.

	Revolutions	200–299	300–399	700–799	900–999
Parameter	Units				
3–50 keV flux	10^{-9} erg cm^{-2} s^{-1}	0.84 ± 0.04	$0.80^{+0.06}_{-0.05}$	0.84 ± 0.05	$0.94^{+0.09}_{-0.08}$
Γ		$1.25^{+0.14}_{-0.17}$	$1.16^{+0.17}_{-0.21}$	$0.98^{+0.20}_{-0.52}$	1.2 (frozen)
$E_{\rm cut}$	keV	$13.0^{+3.9}_{-1.9}$	$15.0^{+6.7}_{-2.6}$	13^{+7}_{-4}	$12.4^{+1.4}_{-2.0}$
$E_{\rm fold}$	keV	$13.6^{+2.2}_{-2.3}$	$11.3^{+2.8}_{-4.3}$	$10.6^{+2.4}_{-3.5}$	12.4 ± 3.0
$A_{\rm smooth}$	10^{-3} ph cm^{-2} s^{-1}	<11.0	<20.0	<21.0	<52.0
$E_{\rm cyc}$	keV	$21.8^{+0.8}_{-0.9}$	$21.6^{+0.9}_{-0.7}$	$20.7^{+1.1}_{-1.5}$	$23.0^{+1.4}_{-1.5}$
$\sigma_{\rm cyc}$	keV	$2.8^{+1.5}_{-1.2}$	$2.8^{+1.4}_{-1.7}$	$4.1^{+2.6}_{-1.5}$	3.0 (frozen)
$\tau_{\rm cyc}$		$0.44^{+0.23}_{-0.13}$	$0.73^{+0.38}_{-0.25}$	$0.57^{+0.45}_{-0.19}$	$0.54^{+0.44}_{-0.27}$
$\tau_{\rm harm}$		$1.4^{+0.7}_{-0.6}$	<1.6	<1.2	<1.3
ISGRI constant		$1.02^{+0.12}_{-0.10}$	$0.91^{+0.19}_{-0.15}$	$0.81^{+0.14}_{-0.12}$	$1.01^{+0.40}_{-0.26}$
$\chi^2_{\rm red}$ (dof)		1.13 (15)	0.90 (16)	0.87 (16)	0.72 (17)

with a standard deviation of 0.5 keV across all 50 spectra, compared to 20.7 ± 0.3 keV in the real *RXTE* data – i.e. *Suzaku* is not systematically likely to measure higher CRSF energies compared to *RXTE*, given the same underlying spectrum. However, this simulated approach does not account for any additional instrumental systematics – these results mainly tell us that the more limited energy range covered by *Suzaku* does not contribute to overall changes in the measured CRSF energy.

Our reported values use HXD/PIN data with a lower limit of 15 keV and XIS data with an upper limit of 12 keV. While these instruments are usually considered to be reliable in these ranges, their calibration is more poorly constrained as one approaches the edges of their energy bounds. We thus checked our results by fitting the phase-averaged *Suzaku* spectra with the PIN limited to above 18 keV and the XIS limited to below 10 keV. Using these limits, we still find results consistent with our reported values. However, the PIN normalization and cutoff energy are considerably less well-constrained, at $1.2^{+0.3}_{-0.4}$ and $17.8^{+5.1}_{-0.7}$ keV, respectively.

The real *Suzaku* spectrum is still fitted fairly well when the CRSF energy is frozen to a typical *RXTE* value – fixing the CRSF energy to 20.7 keV results in a reduced χ^2 value of 1.29 for 522 degrees of freedom, compared to 1.25 for 521 DOF when the CRSF is left free to vary, with a reduction in χ^2 of 19.3. This fit also brings the cutoff energy $E_{\rm cut}$ more into line with the measured values found using *RXTE*. However, the F-test probability for this improvement to arise by chance is 3.1×10^{-5}.

It should be noted that in the phase-averaged *Suzaku* spectra, the cutoff energy is very high compared to *RXTE* and relatively close to the CRSF energy (18.6 keV for $E_{\rm cut}$ versus 22.7 keV for $E_{\rm cyc}$). The depth of the 'smoothing' Gaussian added to compensate for the piecewise nature of the `plcut` continuum is also quite high compared to the *RXTE* values. This is likely in part due to the energy gap between the XIS and HXD/PIN spectra – if the smoothing Gaussian is omitted entirely, the cutoff energy and CRSF energy are both found at nearly the same energy, at ∼21–22 keV.

There is no detectable correlation between $E_{\rm cut}$ and $E_{\rm cyc}$ in the combined *RXTE*, *INTEGRAL*, and *Suzaku* data sets. However, Fig. 9 shows confidence contours for $E_{\rm cyc}$ versus $E_{\rm cut}$ for *Suzaku* and the 123–140 count s^{-1} *RXTE* data, which is closest in flux to the *Suzaku* measurements; while the *RXTE* results are highly inconsistent with *Suzaku*, the *Suzaku* contours are strangely shaped, with a noticeable correlation between $E_{\rm cyc}$ and $E_{\rm cut}$ above $E_{\rm cut} \approx 20$ keV. This correlation is likely artificial, due to the piecewise continuum; the fact that the best-fitting value lies in the 'spike' above the correlated region suggests that the measured value can be trusted.

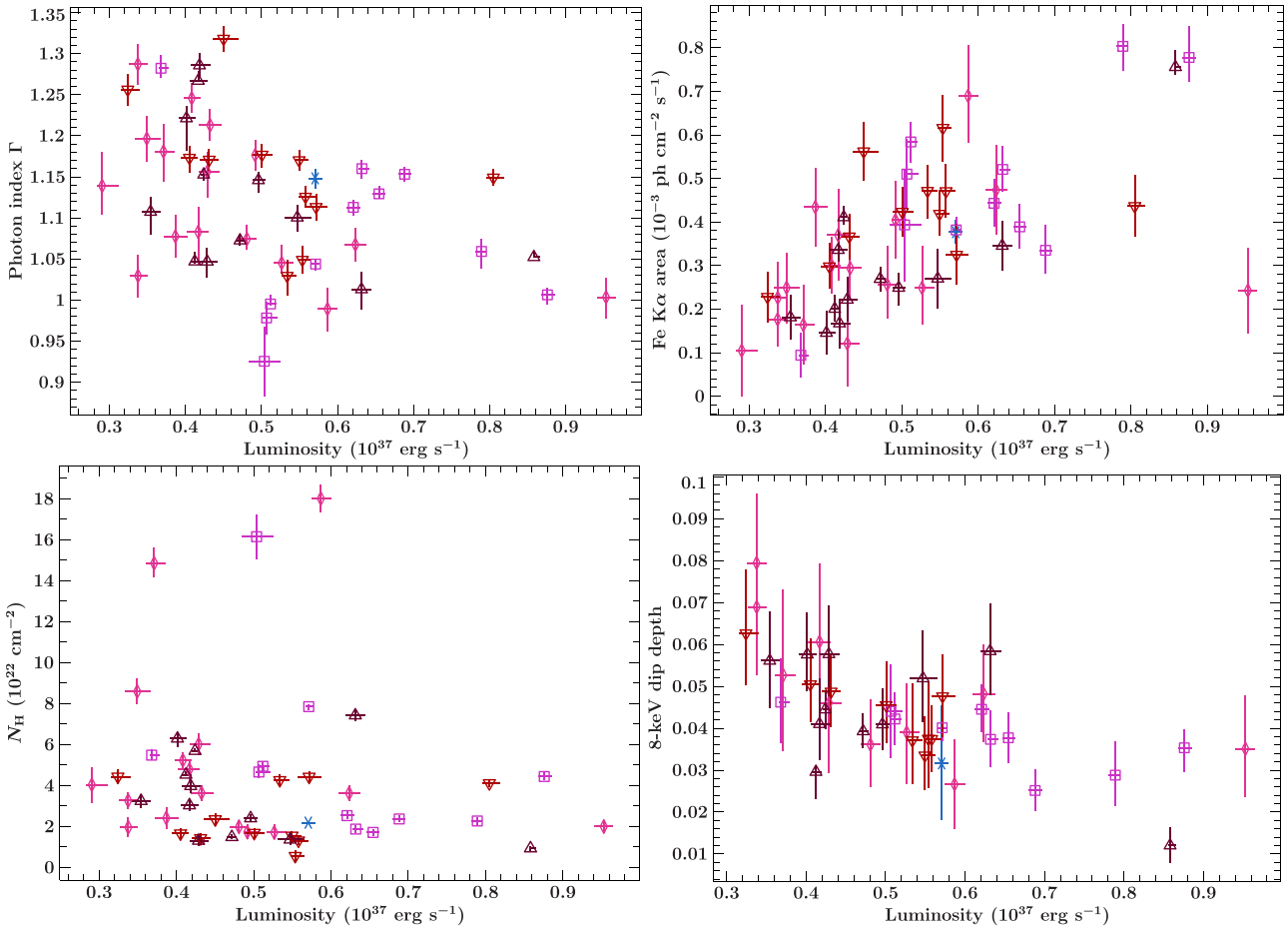

Figure 4. Clockwise from upper left: power-law index Γ, iron line flux, 8-keV feature optical depth, and absorbing column density N_H from the obsid-by-obsid data set using the `mplcut` continuum, plotted against luminosity. *RXTE* measurements are in dark red triangles, red inverted triangles, violet squares, and pink diamonds for proposals P10145, P20146, P50067, and P80016, respectively, while the *Suzaku* measurement is plotted as a blue star.

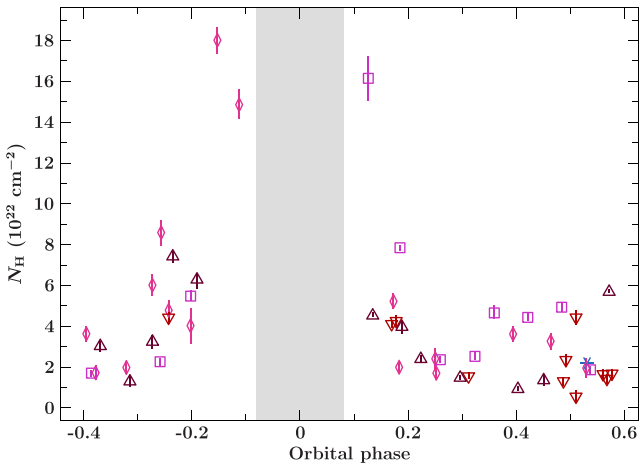

Figure 5. The absorbing column density towards 4U 1538−522 plotted against orbital phase, using the orbital parameters from Table 2. The approximate extent of the X-ray eclipse is shaded; phase 0.0 is the eclipse centre. Symbols and colours are as in Fig. 4.

We can get some additional insight as to the difference between the *Suzaku* and *RXTE* spectra by examining different models and different data sets. Fitting the pulse-by-pulse and obsid-by-obsid data sets with the `fdcut` continuum still finds a significantly higher E_{cyc}, at $22.8^{+0.5}_{-0.3}$, compared to ∼21.2 keV in *RXTE*. However, the cutoff energy found with *Suzaku* using `fdcut` is still significantly higher than the *RXTE* measurement (26.5 ± 1.2 keV compared to ∼22 keV in *RXTE*), and the confidence contours in both *RXTE* and *Suzaku* are not as well constrained as with the `mplcut` continuum.

The most interesting result is that of the phase-constrained *Suzaku* spectrum of the peak of the main pulse, which does not suffer from the same issues as the phase-averaged spectrum does – using `mplcut`, its spectral parameters including E_{cut} are entirely consistent with the *RXTE* values, with the exception of its CRSF energy, which at $23.0^{+0.9}_{-0.8}$ is significantly higher than the ∼20.9 found in the *RXTE* spectra. This can be seen clearly in the left-hand panel of Fig. 7. Fig. 10 shows the E_{cut}–E_{cyc} contours for the peak-pulse spectra; in this case *Suzaku* clearly finds a higher energy CRSF compared to *RXTE*. There is some bimodality in the contours with a very slightly lower energy CRSF at a significantly higher cutoff energy, but this is still a significantly higher energy CRSF compared to *RXTE*. This raises the possibility that the increased CRSF energy seen in the phase-averaged data is due primarily to an increase in the CRSF energy in this phase bin. Indeed, the spectra of the *secondary* pulse do not show any evolution of the CRSF in time (see the right-hand panel of Fig. 7); this could be due to a change in accretion geometry limited to a single pole. However, it should be noted that the *Suzaku* spectrum of the secondary peak has a very poorly constrained cutoff energy.

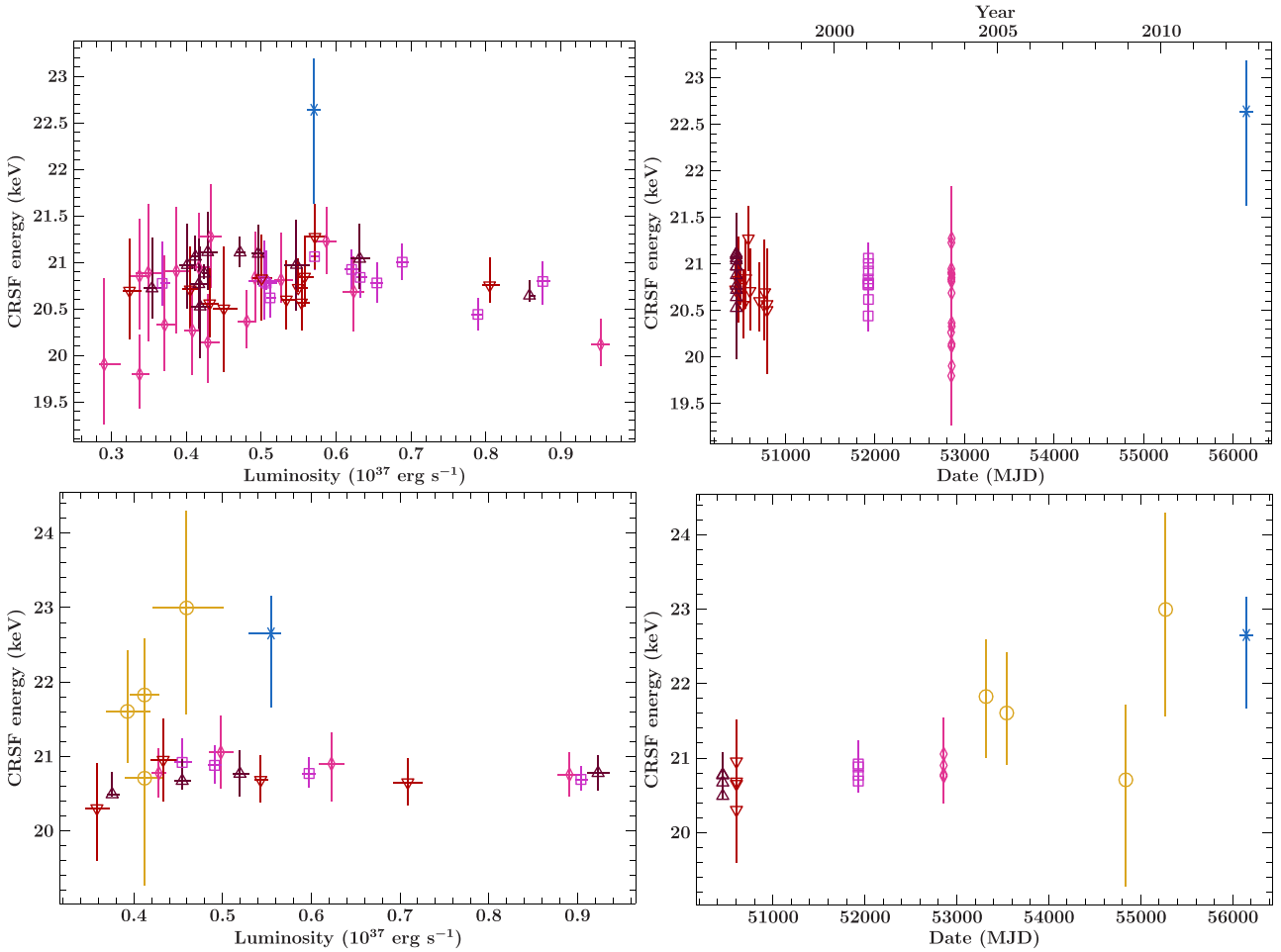

Figure 6. 4U 1538−522's CRSF energy using the `mplcut` continuum and phase-averaged data. Upper plots display the results from the individual obsids, while the lower panels display the pulse-by-pulse results. Left-hand plots have the CRSF energy plotted against 3–50 keV flux, and right-hand plots show the energy plotted against time. Symbols and colours are as in Fig. 4, with *INTEGRAL* results plotted in gold circles.

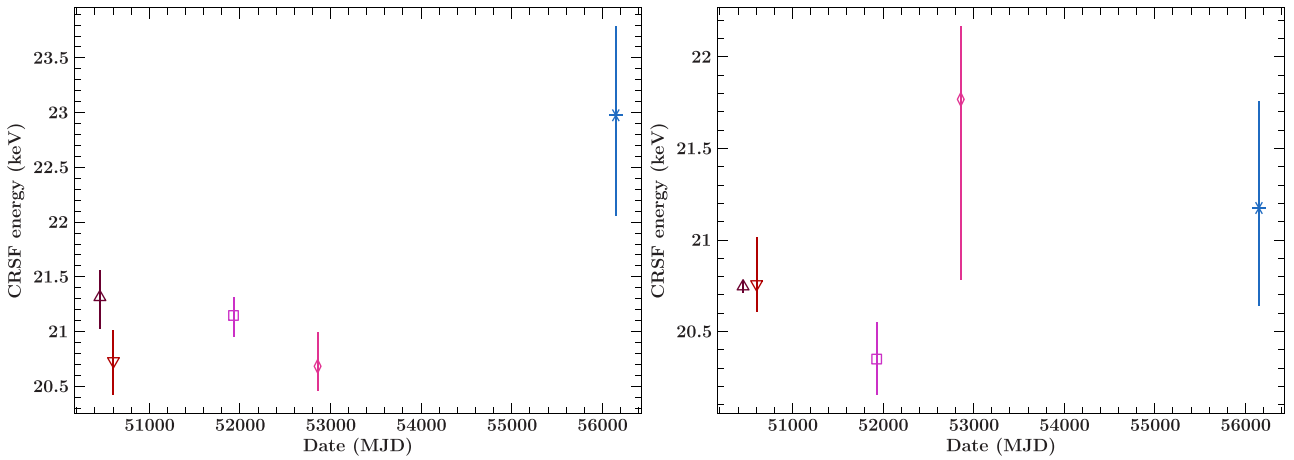

Figure 7. 4U 1538−522's CRSF energy from the phase-resolved data sets, both plotted against time. On the left, the measurements from the peak of the main pulse; on the right are the measurements from the secondary pulse. The large increase in CRSF energy seen in the main-pulse spectrum is not apparent in the spectrum of the secondary pulse.

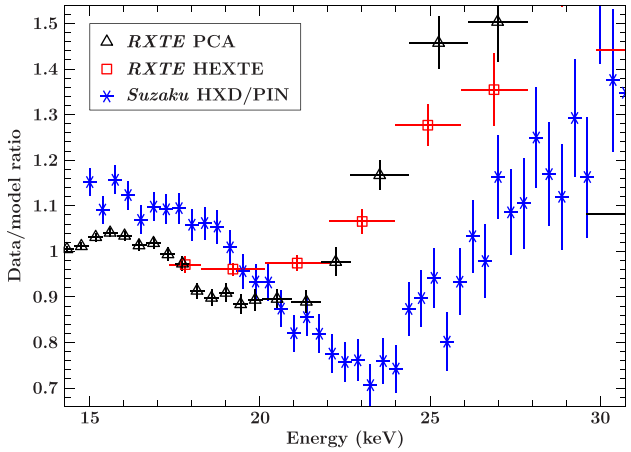

Figure 8. The ratio residuals for a fit with no CRSF for the 140–171 count s^{-1} flux bin *RXTE* proposal P50067 and the *Suzaku* observation (i.e. the same data as in Fig. 3) in the 15–30 keV band. The PCA data are shown in black triangles, the HEXTE in red squares, and the PIN in blue stars. The CRSF energy in the *Suzaku* observation is clearly higher than in the *RXTE* data.

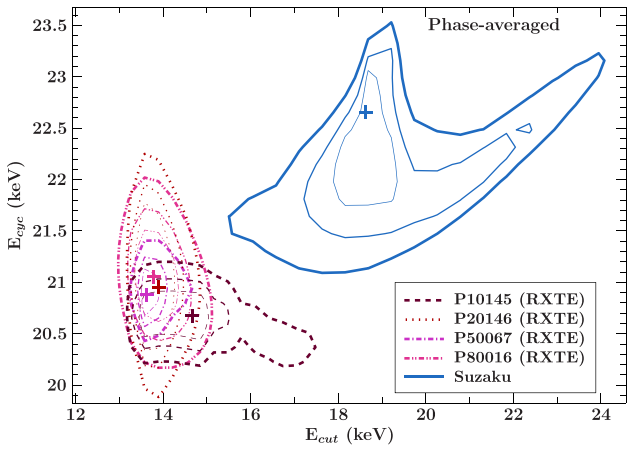

Figure 9. $E_{\rm cut}$ versus $E_{\rm cyc}$ contours for *Suzaku* and the 123–140 count s^{-1} *RXTE* results, using phase-averaged spectra. From the inside out, the contours represent the 68, 90, and 99 per cent confidence intervals for two parameters. See text for details regarding the interpretation of the *Suzaku* contours.

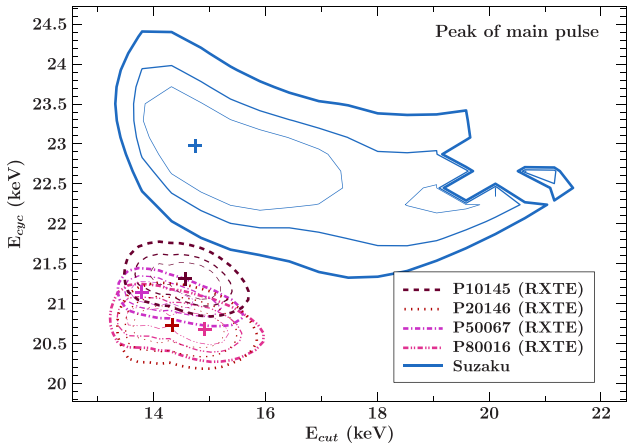

Figure 10. $E_{\rm cut}$ versus $E_{\rm cyc}$ contours for *Suzaku* and *RXTE* spectra of the peak of the main pulse. Confidence intervals are same as in Fig. 9.

6 DISCUSSION

6.1 Relationship between $E_{\rm cyc}$ and flux

There are two generally recognized regimes for NS accretion, originally laid out by Basko & Sunyaev (1976), defined by the critical luminosity $L_{\rm crit}$. When accretion is supercritical, radiation pressure is capable of stopping the infalling material entirely; in this case, the accreted material sinks relatively slowly from a radiation-dominated shock to the surface, and the observed X-rays are mainly photons that escape through the sides of the column ('fan-beam' emission), as the optical depth through the top of the column is large. Under subcritical accretion, for luminosities significantly below $L_{\rm crit}$, the infalling material impacts on and heats the surface (Zel'dovich & Shakura 1969), producing an accretion mound and a hotspot at the magnetic pole; here, the observed X-rays can escape from the top of the column ('pencil-beam' emission) due to the lower optical depth of the weaker accretion stream. In the transition region between these two modes, when the accretion is still subcritical but close to the critical point, the infalling material is likely slowed by a combination of radiation pressure and gas pressure, and the emission is a hybrid of the above two modes.

Becker et al. (2012) and Poutanen et al. (2013) present two very different mechanisms for CRSF production and variability. Becker et al. (2012) has the CRSF being produced directly in the accretion channel, and the observed correlations derive from the line-producing region moving upwards (when accretion is supercritical) or downwards (for moderately subcritical accretion) in the column in response to increases in accretion rate. In contrast, the CRSF in the Poutanen et al. (2013) model is produced when light from the accretion column, which is preferentially beamed downwards due to relativistic effects, reflects off the stellar surface, with the CRSF energy determined by the surface magnetic field strength of the NS. Under supercritical accretion, the height of the accretion column is proportional to the accretion rate, and thus the observed $E_{\rm cyc}$–luminosity anticorrelation results the taller column illuminating a larger fraction of the NS surface, sampling a lower average magnetic field (as the surface magnetic field strength drops as one moves away from the magnetic pole). Both models make similar qualitative predictions for the supercritical case, but the reflection model inherently predicts smaller variations in $E_{\rm cyc}$, as the magnetic field only varies by a factor of $\sim$2 over the NS surface (compared to $B \propto r^{-3}$ in the higher reaches of the column). While Poutanen et al. (2013) do not directly address the subcritical-accretion case in their work, highly subcritical sources will emit their X-rays from a hotspot on the surface, and the reflection mechanism is not likely to produce strong variability in these cases. Moderately-subcritical sources will still have something approximating an accretion column; for these cases, Mushtukov et al. (2015b) point out that the velocity distribution of infalling electrons will change as a source goes from highly subcritical to moderately subcritical, with the electron velocity at the base of the accretion channel reaching zero when the source reaches critical luminosity. The change in the distribution of Doppler shifts between photons and electrons as the source approaches $L_{\rm crit}$ then results in the observed positive trend between $E_{\rm cyc}$ and luminosity.

Assuming the NS mass and radius are 1 $M_\odot$ (Rawls et al. 2011) and 10 km, respectively, and assuming spherical accretion, the theoretical framework laid out by Becker et al. (2012) finds that the effective Eddington luminosity, $L_{\rm crit}$, is 1.0×10^{36} erg s^{-1}, somewhat lower than 4U 1538−522's typical luminosity range of 3–10×10^{36} erg s^{-1}. One can adjust the predicted $L_{\rm crit}$ up and down

depending on the parameters one chooses; however, there is no physically reasonable set of parameters that results in 4U 1538−522 accreting subcritically for more than a small fraction of its observed luminosity range – pushing $L_{\rm crit}$ to above $\sim 5 \times 10^{36}$ erg s^{-1} would require either assuming disc accretion or assuming that the surface magnetic field strength is significantly higher than CRSF energy predicts.

Thus, this implies that 4U 1538−522 accretes supercritically, and we should thus expect a negative $E_{\rm cyc}$–luminosity correlation. This can only be reconciled with observations if the predicted change in $E_{\rm cyc}$ is small enough to be hidden in the available data, which, with some dependence on the data set one looks at, constrains us to changes of $\sim$0.1 keV per 10^{36} erg s^{-1}. Becker et al. (2012) find a linear relationship between luminosity and the height of the CRSF-producing region for supercritical accretion, thus predicting a change in height by a factor of $\sim$3 for 4U 1538−522. The exact height depends on the value of the ξ parameter from Becker et al. (2012), which characterizes the relationship between the flow velocity of the accreted material and the effective 'velocity' of photon diffusion upwards through the infalling material; taking ξ to be $\sim 10^{-2}$ results in emission heights of $\sim$10–30 m above the NS surface. If one assumes a dipolar magnetic field, this range of heights corresponds to a change in the CRSF energy of the order of 10^{-2}–10^{-3} keV, far smaller than any observable trend. However, the magnetic field this close to the NS surface may deviate significantly from a dipole (see e.g. Mukherjee & Bhattacharya 2012), so this prediction should be viewed with some care.

More recent work by Mushtukov et al. (2015a) attempts to additionally take into account resonant scattering and photon polarization. Their work finds that wind-accreting sources generally have *higher* $L_{\rm crit}$ compared to disc-accreting sources, due to the larger footprint of the accretion flow. While they do not provide calculations for 4U 1538−522's exact parameters, they do find $L_{\rm crit} \approx$ 2–4 $\times$ 10^{36} erg s^{-1} for wind-accreting sources around 4U 1538−522's CRSF energy, intriguingly close to the $\sim 6 \times 10^{36}$ erg s^{-1} 'break' in the $E_{\rm cyc}$–luminosity relationship seen in the obsid-by-obsid data set. Mushtukov et al. (2015a) assume an NS mass of 1.4 M$_\odot$, while 4U 1538−522's NS is likely closer to $\sim$1 M$_\odot$. A lower mass would result in a lower velocity for infalling material, decreasing $L_{\rm crit}$, but would also increase the size of the hotspot on the NS surface, decreasing the temperature of the hotspot and increasing $L_{\rm crit}$. The overall effect here is difficult to judge, given the lack of a closed-form solution using the framework of Mushtukov et al. (2015a).

There are a number of systematic factors that can influence the calculated luminosity, which must be taken into account if we are to compare our results to theoretical predictions. The uncertainty in the distance to 4U 1538−522 is $\sim$1 kpc, corresponding to at most a factor of $\sim$2 possible change in the measured luminosity; if the distance is closer to Clark (2004)'s estimate of 4.5 kpc, our observed luminosity range is closer to 1.5–4.5 $\times$ 10^{36} erg s^{-1}. Relativistic lightbending and the non-isotropic emission of the X-ray pulsar will also push the true luminosity down, since our luminosity calculation assumes emission over 4π sr; when this beaming is taken into account, the true luminosity can be a factor of $\sim$2 lower compared to the computed luminosity, although this is highly dependent on the emission geometry (M. Kühnel, private communication; Martínez-Núñez et al., in preparation). Overall, though, the lack of any detectable trend, the weakness of the predicted correlations, and the possible close proximity of the scattering region to the NS surface make it prudent to say at this stage that 4U 1538−522's accretion mode is still uncertain.

6.2 Change in $E_{\rm cyc}$ between *RXTE* and *Suzaku*

The CRSF energy of 4U 1538−522 appears to have increased between the *RXTE* measurements of 1996–2004 and the 2012 *Suzaku* measurement. This is a peculiar occurrence; while it does not seem entirely attributable to instrumental or modelling artefacts, it may be limited to the peak of the main pulse.

We plot all $E_{\rm cyc}$ measurements for 4U 1538−522 in Fig. 11. Robba et al. (2001), analysing the 1998 *BeppoSAX* observation of 4U 1538−522, found a phase-averaged CRSF energy of 21.1 $\pm$ 0.2 keV, entirely in line with the *RXTE* measurements from around the same time. The *BeppoSAX* analysis used approximately the same model choices as this analysis (`plcut` continuum and a `gauabs` CRSF) and found the source at a roughly comparable luminosity to the average *RXTE* luminosity. It is somewhat more difficult to compare the results of the 1988 and 1990 *Ginga* observations (Clark et al. 1990; Mihara 1995), when the CRSF was discovered, due to differences in model choice. The Clark et al. analysis used a model consisting of a power-law modified by a

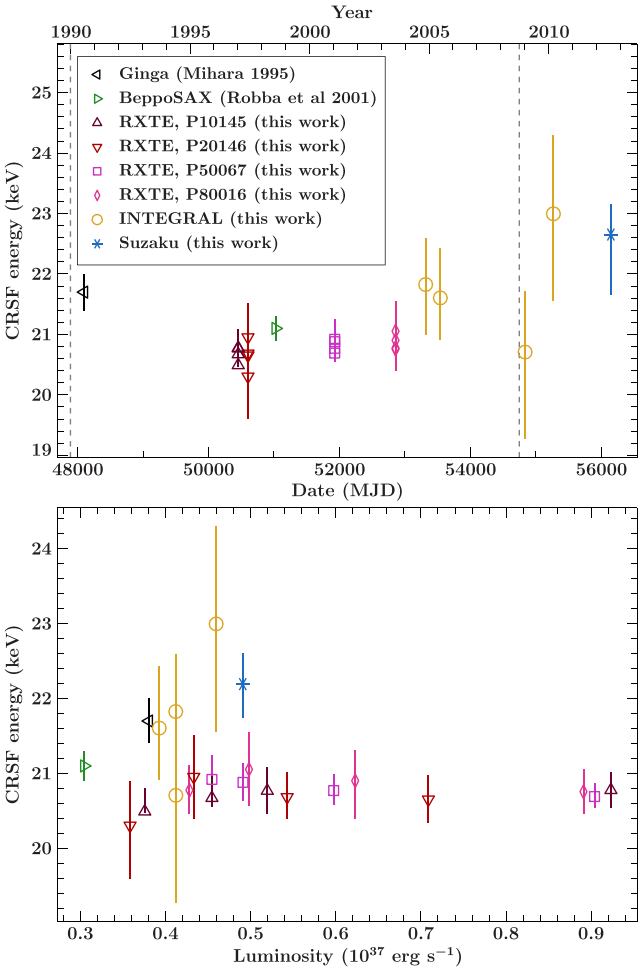

Figure 11. 22 yr of $E_{\rm cyc}$ measurements for 4U 1538−522 versus time (left-hand panel) and versus luminosity (right-hand panel). Luminosity is calculated from the 3–50 keV flux, taking spectral parameters from the best-fitting phase-averaged models used by Mihara (1995) and Robba et al. (2001). All measurements use Gaussian profiles for the CRSF. The approximate times for 4U 1538−522's torque reversals in 1990 and late 2008 are indicated by vertical dashed lines.

`cyclabs` component, where the second harmonic in the `cyclabs` model effectively modelled the high-energy turnover that we model using `highecut`. Mihara introduced the `npex` continuum model and compared different CRSF models (see table F.1.1 in Mihara 1995). Using a Gaussian optical depth profile for the CRSF, he found an energy of 21.7 ± 0.3 keV (the usually quoted value is 20.6 keV, but this uses the `cyclabs` model, where the fitted energy does not correspond to the peak energy of the CRSF). Applying the same procedure as we used for the significance of the *Suzaku* point, the *Ginga* measurement sits above the *RXTE* average, but at only 2.1σ, the separation is not as great as the *RXTE-Suzaku* split.

Currently, Her X-1 is the only source with confirmed long-term evolution in its CRSF independent of other observable factors (Staubert et al. 2014; Klochkov et al. 2015). Its CRSF behaviour with respect to time displays two main features: a sharp jump upwards by ∼4 keV in the early 1990s, followed by an ∼0.25 keV yr^{-1} decline since then. Additionally, a 2012 *INTEGRAL* observation found a significantly higher CRSF energy compared to the surrounding *Suzaku*, *INTEGRAL*, and *NuSTAR* observations, indicating that significant changes in the CRSF energy can occur on both short and long time-scales.

In 4U 1538−522's case, the *RXTE* and *BeppoSAX* data are bracketed by higher energy measurements from *Suzaku* and *Ginga*. The *RXTE* and *BeppoSAX* measurements alone cannot constrain any trend with time; however, a linear fit to the *RXTE*, *BeppoSAX*, *INTEGRAL*, and *Suzaku* measurements finds a slope of 0.058 ± 0.014 keV yr^{-1}. However, the large uncertainties on the *INTEGRAL* measurements make it impossible to say for certain whether the *Suzaku* measurement represents a long-term trend or merely a short-term increase in $E_{\rm cyc}$.

It is highly unlikely that we are observing the evolution of the NS's intrinsic magnetic field; rather, any long-term change in the CRSF energy is likely due to a change in the properties of the scattering region where the CRSF is produced. We have discussed some of the properties of the scattering region above in Section 6.1; the question now is how one can produce an ∼1 keV shift in the CRSF energy alongside minimal long-term changes in the source flux given the properties of the accretion flow.

4U 1538−522 is a young system, as indicated by its high-mass B0Iab companion and its strong magnetic field, so it is unlikely that accretion has been ongoing long enough to significantly 'bury' the magnetic field (in the sense outlined by Payne & Melatos 2004); this burial process proceeds on far too long of a time-scale to produce a change of a few per cent in only a few years. However, Mukherjee & Bhattacharya (2012) find that accretion mound masses of $\sim 10^{-12}$ M$_\odot$ are likely sufficient to distort the magnetic field significantly. Based on the observed CRSF energy–luminosity relationship as discussed in Section 6.1, the CRSF parameters are probably a good probe of the environment around the polar cap, and a change in the CRSF parameters could reflect some changes in the accretion mound which might not be visible in other observables, such as luminosity. For example, a slow growth in the mound's height would probably not affect the broad-band spectral parameters or luminosity of 4U 1538−522 very much (the mound mainly contributes to the blackbody component of the spectrum, which is a small fraction of the source's overall luminosity; see e.g. Becker & Wolff 2007). However, relatively small changes in the mound's height can affect the magnetic field in the mound quite drastically – Mukherjee & Bhattacharya (2012) found that the magnetic field strength could deviate from the dipole strength by upwards of a factor of 4 in the sides of sufficiently large accretion mounds. An ∼5 per cent increase in 4U 1538−522's CRSF energy could be simply due to a reconfiguring of the mound geometry resulting in a slightly stronger average field strength. However, it is unclear as to whether a 5–10 year time-scale is realistic for this type of process. Also, as pointed out above, it is unclear if the shift observed by *Suzaku* is representative of a long-term change in the CRSF energy or if it is more of a temporary effect.

There is the additional question of whether the change in the CRSF energy is related to a change in only one of the accretion columns, or if it is due to changes in both columns. The fact that the changed CRSF energy is most prominent in the phase-constrained data from the peak of the main pulse and not detected in the secondary pulse suggests that this effect may be limited to a single magnetic pole. Given the possible mechanisms laid out above, this is not an unreasonable thing to suggest – there is no fundamental reason that the two poles' accretion structures should move in lockstep with each other; a difference of a few per cent in the two poles is conceivable.

Finally, it is interesting to note here that the source underwent torque reversals in ∼1990 (Rubin et al. 1997) and ∼2008 (Finger et al. 2009; Hemphill et al. 2013), intriguingly close to bracketing the *RXTE* and *BeppoSAX* observations and separating them somewhat from the higher-energy *Ginga* and *Suzaku* measurements. For an accreting NS, the evolution of the spin period is driven by the torque exerted on the NS's magnetic field by the accreted material; thus it is reasonable to say that a shift in the properties of the magnetic field could be associated with changes in the pulse period evolution. Unfortunately, there is no spectrally sensitive coverage of either torque reversal; the best we can do is look at the *INTEGRAL* results of (Hemphill et al. 2013), which found no significant changes on either side of the 2008 torque reversal. However, *INTEGRAL*'s relative spectral insensitivity means there is ample room for smaller changes. The *RXTE* All-Sky Monitor (ASM) (Levine et al. 1996) shows no detectable changes in flux in this time, although 4U 1538−522 is very dim in the ASM – rebinning the ASM light curve to the 3.74 d orbital period, the counting rate is 0.7 ± 0.8 count s^{-1} – and as such we cannot place any strong limits on source variability across the torque reversal based on the ASM light curve.

7 CONCLUSION

We have performed a comprehensive analysis of ∼15 yr of X-ray observations of the high-mass X-ray binary 4U 1538−522, using data from the *RXTE*, *Suzaku*, and *INTEGRAL* satellites. Spectrally, the source is relatively stable, with the continuum parameters remaining mostly flat with respect to changes in luminosity. The main results are the lack of a significant correlation between the centroid energy of the fundamental CRSF and the increase by ∼1 keV in the CRSF energy between the *RXTE* and *Suzaku* observations. The lack of a detectable correlation between the CRSF energy and luminosity is supported by theoretical work by Becker et al. (2012), Poutanen et al. (2013), and Mushtukov et al. (2015a), although there is some uncertainty as to exactly what theoretical scenario is being played out. The time-dependence of the CRSF is a less easily understood issue and requires additional work to, first, confirm or deny its reality and secondly, produce a reliable explanation for the phenomenon. An upcoming *INTEGRAL* campaign will help shed some light on the first point, but what are truly needed are observations by more spectrally sensitive instruments, e.g. those aboard *NuSTAR* or *Astro-H*, which will be able to make a precise measurement of the CRSF energy.

ACKNOWLEDGEMENTS

This research has made use of data and/or software provided by the High Energy Astrophysics Science Archive Research Center (HEASARC), which is a service of the Astrophysics Science Division at NASA/GSFC and the High Energy Astrophysics Division of the Smithsonian Astrophysical Observatory. Our analysis makes heavy use of a collection of ISIS scripts provided by ECAP/Remeis Observatory and MIT, which can be found at http://www.sternwarte.uni-erlangen.de/isis/. Support for VG was provided by NASA through the Smithsonian Astrophysical Observatory (SAO) contract SV3-73016 to MIT for Support of the Chandra X-Ray Center (CXC) and Science Instruments; CXC is operated by SAO on behalf of NASA under contract NAS8-03060.

REFERENCES

Basko M. M., Sunyaev R. A., 1976, MNRAS, 175, 395
Baykal A., İnam S. C., Beklen E., 2006, A&A, 453, 1037
Becker P. A., Wolff M. T., 2007, ApJ, 654, 435
Becker R. H., Swank J. H., Boldt E. A., Holt S. S., Serlemitsos P. J., Pravdo S. H., Saba J. R., 1977, ApJ, 216, L11
Becker P. A. et al., 2012, A&A, 544, A123
Bradt H. V., Rothschild R. E., Swank J. H., 1993, A&AS, 97, 355
Caballero I. et al., 2007, A&A, 465, L21
Clark G. W., 2000, ApJ, 542, L131
Clark G. W., 2004, ApJ, 610, 956
Clark G. W., Woo J. W., Nagase F., Makishima K., Sakao T., 1990, ApJ, 353, 274
Coburn W., 2001, PhD thesis, Univ. California, San Diego
Coburn W., Heindl W., Rothschild R., Gruber D., Kreykenbohm I., Wilms J., Kretschmar P., Staubert R., 2002, ApJ, 580, 394
Corbet R. H. D., Woo J. W., Nagase F., 1993, A&A, 276, 52
Crampton D., Hutchings J. B., Cowley A. P., 1978, ApJ, 225, L63
Davison P. J. N., 1977, MNRAS, 179, 35P
Davison P. J. N., Watson M. G., Pye J. P., 1977, MNRAS, 181, 73
Dickey J. M., Lockman F. J., 1990, ARA&A, 28, 215
Falanga M., Bozzo E., Lutovinov A., Bonnet-Bidaud J. M., Fetisova Y., Puls J., 2015, A&A, 577, A130
Ferrigno C., Becker P. A., Segreto A., Mineo T., Santangelo A., 2009, A&A, 498, 825
Finger M. H. et al., 2009, in Johnson W. N., Thompson D. J., eds, Fermi Symp. eConf. Proc. C0911022, Washington, DC, preprint (arXiv:0912.3847)
Fürst F. et al., 2013, ApJ, 779, 69
Fürst F. et al., 2014, ApJ, 780, 133
Giacconi R., Murray S., Gursky H., Kellogg E., Schreier E., Matilsky T., Koch D., Tananbaum H., 1974, ApJS, 27, 37
Hemphill P. B., Rothschild R. E., Caballero I., Pottschmidt K., Kühnel M., Fürst F., Wilms J., 2013, ApJ, 777, 61
Hemphill P. B., Rothschild R. E., Markowitz A., Fürst F., Pottschmidt K., Wilms J., 2014, ApJ, 792, 14
Houck J. C., Denicola L. A., 2000, in Manset N., Veillet C., Crabtree D., eds, ASP Conf. Ser. Vol. 216, Astronomical Data Analysis Software and Systems IX. Astron. Soc. Pac., San Francisco, p. 591
Ilovaisky S. A., Chevalier C., Motch C., 1979, A&A, 71, L17
Jahoda K., Swank J. H., Giles A. B., Stark M. J., Strohmayer T., Zhang W., Morgan E. H., 1996, in Siegmund O. H., Gummin M. A., eds, Proc. SPIE Conf. Ser. Vol. 2808, EUV, X-Ray, and Gamma-Ray Instrumentation for Astronomy VII. SPIE, Bellingham, p. 59
Jahoda K., Markwardt C. B., Radeva Y., Rots A. H., Stark M. J., Swank J. H., Strohmayer T. E., Zhang W., 2006, ApJS, 163, 401
Kalberla P. M. W., Burton W. B., Hartmann D., Arnal E. M., Bajaja E., Morras R., Pöppel W. G. L., 2005, A&A, 440, 775
Klochkov D., Staubert R., Santangelo A., Rothschild R. E., Ferrigno C., 2011, A&A, 532, A126
Klochkov D. et al., 2012, A&A, 542, L28
Klochkov D., Staubert R., Postnov K., Wilms J., Rothschild R. E., Santangelo A., 2015, A&A, 578, A88
Koyama K. et al., 2007, PASJ, 59, 23
Kreykenbohm I., Coburn W., Wilms J., Kretschmar P., Staubert R., Heindl W. A., Rothschild R. E., 2002, A&A, 395, 129
Leahy D. A., Darbro W., Elsner R. F., Weisskopf M. C., Kahn S., Sutherland P. G., Grindlay J. E., 1983, ApJ, 266, 160
Levine A. M., Bradt H., Cui W., Jernigan J. G., Morgan E. H., Remillard R., Shirey R. E., Smith D. A., 1996, ApJ, 469, L33
Makishima K., Koyama K., Hayakawa S., Nagase F., 1987, ApJ, 314, 619
Mihara T., 1995, PhD thesis, Univ. Tokyo
Mowlavi N. et al., 2006, A&A, 451, 187
Mukherjee D., Bhattacharya D., 2012, MNRAS, 420, 720
Mukherjee U., Raichur H., Paul B., Naik S., Bhatt N., 2006, J. Astrophys. Astron., 27, 411
Müller S. et al., 2012, A&A, 546, A125
Müller S. et al., 2013a, A&A, 551, A6
Müller D., Klochkov D., Caballero I., Santangelo A., 2013b, A&A, 552, A81
Mushtukov A. A., Suleimanov V. F., Tsygankov S. S., Poutanen J., 2015a, MNRAS, 447, 1847
Mushtukov A. A., Tsygankov S. S., Serber A. V., Suleimanov V. F., Poutanen J., 2015b, MNRAS, 454, 2714
Nowak M. A., Wilms J., Pottschmidt K., Schulz N., Maitra D., Miller J., 2012, ApJ, 744, 107
Payne D. J. B., Melatos A., 2004, MNRAS, 351, 569
Poutanen J., Mushtukov A. A., Suleimanov V. F., Tsygankov S. S., Nagirner D. I., Doroshenko V., Lutovinov A. A., 2013, ApJ, 777, 115
Rawls M. L., Orosz J. A., McClintock J. E., Torres M. A. P., Bailyn C. D., Buxton M. M., 2011, ApJ, 730, 25
Reynolds A. P., Bell S. A., Hilditch R. W., 1992, MNRAS, 256, 631
Robba N. R., Burderi L., Di Salvo T., Iaria R., Cusumano G., 2001, ApJ, 562, 950
Rodes-Roca J. J., Torrejón J. M., Kreykenbohm I., Martínez Núñez S., Camero-Arranz A., Bernabéu G., 2009, A&A, 508, 395
Rodes-Roca J. J., Mihara T., Nakahira S., Torrejón J. M., Giménez-García Á., Bernabéu G., 2015, A&A, 580, A140
Rothschild R. E. et al., 1998, ApJ, 496, 538
Rubin B. C., Finger M. H., Scott D. M., Wilson R. B., 1997, ApJ, 488, 413
Sartore N., Jourdain E., Roques J. P., 2015, ApJ, 806, 193
Staubert R., Shakura N. I., Postnov K., Wilms J., Rothschild R. E., Coburn W., Rodina L., Klochkov D., 2007, A&A, 465, L25
Staubert R., Klochkov D., Wilms J., Postnov K., Shakura N. I., Rothschild R. E., Fürst F., Harrison F. A., 2014, A&A, 572, A119
Takahashi T. et al., 2007, PASJ, 59, 35
Tanaka Y., 1986, in Mihalas D., Winkler K.-H. A., eds, Lecture Notes in Physics, Vol. 255, IAU Colloq. 89: Radiation Hydrodynamics in Stars and Compact Objects. Springer-Verlag, Berlin, p. 198
Trümper J., Pietsch W., Reppin C., Voges W., Staubert R., Kendziorra E., 1978, ApJ, 219, L105
Tsygankov S. S., Lutovinov A. A., Serber A. V., 2010, MNRAS, 401, 1628
Vasco D., Klochkov D., Staubert R., 2011, A&A, 532, A99
Vasco D., Staubert R., Klochkov D., Santangelo A., Shakura N., Postnov K., 2013, A&A, 550, A111
Verner D. A., Ferland G. J., Korista K. T., Yakovlev D. G., 1996, ApJ, 465, 487
White N. E., Swank J. H., Holt S. S., 1983, ApJ, 270, 711
Willingale R., Starling R. L. C., Beardmore A. P., Tanvir N. R., O'Brien P. T., 2013, MNRAS, 431, 394
Wilms J., Allen A., McCray R., 2000, ApJ, 542, 914
Wilms J., Lee J. C., Nowak M. A., Schulz N. S., Xiang J., Juett A., 2010, BAAS, 41, 674
Yamamoto T., Sugizaki M., Mihara T., Nakajima M., Yamaoka K., Matsuoka M., Morii M., Makishima K., 2011, PASJ, 63, 751
Zel'dovich Y. B., Shakura N. I., 1969, SvA, 13, 175

This paper has been typeset from a TEX/LATEX file prepared by the author.